

AN ABSTRACT OF THE THESIS OF

Leif J. Steigleder, for the degree of Master of Science in Industrial Engineering, presented on June 14, 2012.

Title: A Microchannel-Based Thermal Management System for Hydrogen Storage Adsorbent Beds.

Abstract Approved: _____

Brian K. Paul

Hydrogen has been shown to be a promising replacement for fossil fuels for use in light duty vehicles because it is a clean, renewable and plentiful resource with a high gravimetric energy density. However, in order to obtain an acceptable volumetric energy density, densification of the hydrogen is required. Adsorptive materials have been shown in the literature to increase volumetric and gravimetric storage densities. A major issue with adsorptive storage is that the adsorption process generates heat and optimal storage conditions are at temperatures below 100 K at pressures up to 50 atm. There is a need to develop heat exchanging architecture that enables adsorbents to be a viable method for hydrogen storage by managing the thermal environment of the storage tank.

Based on previous modeling efforts to determine an acceptable bed module height for removal of heat via microchannel cooling plates, a thermal management system has been designed and tested capable of removing the heat of adsorption within adsorbent-filled

hydrogen storage tanks. The system uses liquid nitrogen cooling to maintain tank temperatures of below 80 K at 50 atm. System studies show that the microchannel architecture offers a high cooling capacity with about a 6% displacement volume. Simulations and experiments have been conducted to evaluate the design for the cooling capacity, pressure drop, and flow distribution between and across the cooling plates, stress due to the pressurized environment, and thermal stress. Cost models have been developed to demonstrate that the system can be manufactured for a reasonable cost at high production volumes. Experimental results show that the modular system offers an acceptable cooling capacity and pressure drop with good flow distribution while adequately managing thermal stresses during operation.

A Microchannel-Based Thermal Management System for Hydrogen Storage Adsorbent Beds

by
Leif J. Steigleder

A THESIS

Submitted to
Oregon State University

in partial fulfillment of
the requirements for the
degree of

Master of Science

Presented June 14, 2012
Commencement June 2013

Master of Science thesis of Leif J. Steigleder presented on June 14, 2012.

APPROVED

Major Professor, Industrial Engineering

Head of the Department of Mechanical, Industrial, and Manufacturing Engineering

Dean of the Graduate School

I understand that this thesis will become a part of the permanent collection of the Oregon State University libraries. My signature below authorizes release of my thesis to any reader upon request.

Leif J. Steigleder, Author

TABLE OF CONTENTS

	<u>Page</u>
1. Introduction	1
2. Background	2
2.1 The Hydrogen Economy.....	2
2.2 Hydrogen Storage	3
2.3 Microchannel Heat Exchangers for Adsorptive Storage.....	7
3. Design	9
3.1 Modular Adsorbent Tank Insert Design.....	13
3.2 Detail Design	18
3.3 Design Evaluation	27
3.3.1 Flow and Thermal Distribution of a Single Cooling Plate	27
3.3.2 Flow Distribution of Multiple Cooling Plates	30
3.3.3 Thermal Effects	32
3.4 Cost Model.....	32
4. Experimental Approach	37
4.1 Prototype Design and Fabrication	37
4.2 Fluidic System Evaluation	44
4.3 Thermal Effects Evaluation	47
5. Experimental Results	49
5.1 Fluidic System Evaluation	49
5.2 Thermal Stress Evaluation	58
6. Conclusions	59
Bibliography	61
APPENDICES	69
APPENDIX A: DOE TECHNICAL HYDROGEN STORAGE TARGETS	70
APPENDIX B: COST REDUCTION STRATEGIES FOR THE MATI	71
APPENDIX C: SHIM CHARACTERIZATION	73

FIGURES

<u>Figure</u>	<u>Page</u>
Figure 1: Geometric concept of the MATI for two adsorbent modules; without modules (left) and with modules (right)	10
Figure 2: Heat exchanging functionality of the MATI with selected design specifications	11
Figure 3: A partial MATI design for four adsorption modules (modules not shown).....	14
Figure 4: Fluid paths of the MATI; liquid nitrogen (cooling plate) and chilled hydrogen (distribution plate).....	15
Figure 5: MATI Manufacturing Plan.....	19
Figure 6: Patterned LN ₂ shims (left) and bonded LN ₂ plate (right).....	20
Figure 7: Top view of LN ₂ etched shim to show pillar geometry, inlet, outlet and ring features	20
Figure 8: Top view of the cooling plate to show the cross section of the header at the inlet joint.....	21
Figure 9: Regions of the cooling plate investigated by FEA.....	22
Figure 10: FEA mesh of the central cooling plate section	22
Figure 11: FEA deflection results of the central cooling plate section	23
Figure 12: H ₂ shims (left) and bonded H ₂ plate (right)	24
Figure 13: Top view of the H ₂ etched shim to highlight header joint and H ₂ pathways	25
Figure 14: Header tube with slits for three cooling plates	26
Figure 15: Header and cooling plate braze joint	26
Figure 16: CFD mesh of the LN ₂ cooling plate inlet (courtesy of Daniel Peterson)	28
Figure 17: Temperature profile of the LN ₂ plate from CFD simulation (courtesy of Daniel Peterson)	29
Figure 18: MATI COGS for 42 plates per bonding cycle at various production volumes.....	34
Figure 19: MATI COGS at high production volumes to show major cost drivers	35
Figure 20: MATI COGS due to processing parameters	36

Figure 21: Design of the MATI prototype with three cooling plates and header tubes.....	38
Figure 22: Design of the top shim and etched shim of the LN2 Plate (left), and design of the header tube (right)	38
Figure 23: Fabricated LN2 shims (PCM and laser cut)	39
Figure 24: Bonded LN2 plates.....	40
Figure 25: Tube machining fixture; setup on a vertical milling machine (top), fixture and clamps (bottom)	41
Figure 26: Vacuum brazing temperature profile	42
Figure 27: Fabricated MATI Prototypes.....	43
Figure 28: Block diagram of the fluidic system evaluation.....	44
Figure 29: Experimental setup for fluidic system evaluation	45
Figure 30: Thermocouple placement for thermal distribution tests (on top side of cooling plate).....	46
Figure 31: Resistive heater placement for cooling capacity and thermal distribution tests (on bottom side of the cooling plate)	47
Figure 32: CFD results for pressure cooling capacity and thermal distribution	49
Figure 33: Thermal results showing the thermocouple groupings.....	51
Figure 34: Thermal profile showing flow distribution of the cooling plates parallel to the flow path.....	52
Figure 35: Thermal profile showing flow distribution of the cooling plates perpendicular to the flow path	53
Figure 36: Temperature difference due to an applied heat load of 52 W at various flow rates	54
Figure 37: Cooling capacity results	55
Figure 38: Pressure drop results of the MATI prototype.....	57
Figure 39: LN2 flow through test.....	59

TABLES

<u>Table</u>	<u>Page</u>
Table 1: Design requirements.....	13
Table 2: Assumptions for MATI system models	15
Table 3: Geometric design specifications	17
Table 4: System model results for displacement volume.....	18
Table 5: Excel model to calculate flow distribution between the cooling plates (courtesy of Daniel Peterson)	30
Table 6: Multi-plate flow distribution results (courtesy of Daniel Peterson).....	31
Table 7: Vacuum brazing cycle.....	42

A MICROCHANNEL-BASED THERMAL MANAGEMENT SYSTEM FOR HYDROGEN STORAGE ADSORBENT BEDS

1. INTRODUCTION

Fossil fuels provide the majority of today's energy for the United States' transportation industry and have been the dominant source of energy for more than a century. Though the country contains less than 5% of the world's population, it demands nearly 25% of the world's fossil fuel production [1]. This presents several challenges for the US economy. One concern with fossil fuels is that nearly 70% of the oil consumed by the United States is imported [1, 2]. The majority of those imports are from countries that are surrounded by increasing political instability, such as Venezuela and countries from Northern Africa and the Middle East [3]. Another issue is that fossil fuels present several environmental and health concerns. Pollutants are generated during the combustion process of converting chemical energy into mechanical energy in automotive applications. One study estimated that around 50% of U.S. citizens live in regions where pollution is concentrated enough to affect public health and the local environment, and transportation is a major contributor to that pollution [4]. Finally, fossil fuels are a finite resource and, therefore, are not renewable. Development of a renewable fuel has the potential to positively impact the US economy, increase energy security, and reduce environmental and health concerns [5, 6].

Hydrogen presents the US with an opportunity to meet all of these challenges. Hydrogen is a resource that can be developed domestically and produces no pollutants when

sourced from renewable power plants (such as wind, solar or hydroelectric) for use with fuel cell vehicles [2,4-6]. Significant funding has been committed towards the development of hydrogen as a fuel since the 1970s to divert a segment of the energy market from fossil fuels [7, 8]. Some researchers estimate that hydrogen-powered vehicles could have up to a 40% share in the US light duty vehicle market by 2050 [5, 7, 8]. By developing and consuming this source of energy domestically, the US will increase its economic and energy security because it will reduce foreign energy dependence [5, 7, 8].

2. BACKGROUND

2.1 The Hydrogen Economy

Hydrogen is the most commonly occurring element in the universe; it is a benign and renewable resource that can be replenished naturally. Because of this, hydrogen has been shown to have great promise because of its availability, renewability, cleanliness, inherent efficiency, and high energy density [5, 7, 8]. One study has shown that the US has the potential to develop enough hydrogen from wind and solar power sources to produce over 15 times the energy needed for light duty vehicles in 2040 [9]. Further, using these energy sources, hydrogen could be produced using water electrolysis without the production of any harmful emissions through the energy's life cycle [2, 5-7, 10].

Well to wheel (WTW) analyses have been conducted by the DOE showing that fuel cell vehicles powered by hydrogen operate at higher efficiency than fossil fuel vehicles and fossil fuel-electric hybrid vehicles [11]. The WTW analysis evaluates the life cycle efficiency of the fuel from development to storage and from storage to consumption. The overall

efficiency includes all losses incurred from production through energy delivery to the wheels of an average light duty vehicle. Fuel cell vehicles using hydrogen fuel showed an efficiency of 36.4% versus 16.7% and 27.3% for gasoline and gasoline-electric powered vehicles, respectively [11]. This is in part due to the fact that fuel cells have the potential to operate at efficiencies of over 60% [10].

While hydrogen has significant promise as a fuel, significant challenges remain in the areas of production, delivery and storage of hydrogen fuel that inhibit its ready acceptance in the transportation industry [5-8, 12]. In particular, storage is a significant challenge due to the volumetric density of hydrogen [12]. Hydrogen has a gravimetric energy density almost four times that of gasoline (120 MJ/kg versus 44 MJ/kg) at standard temperature and pressure [13]. However, under the same conditions, its volumetric energy density is less than 1 MJ/L where fossil fuels are over 30 MJ/L [13].

2.2 Hydrogen Storage

The most prominent issue surrounding hydrogen storage is that gaseous hydrogen has a low physical density. At standard temperature and pressure (STP), 1 kg of hydrogen occupies a volume of 11 m³ (0.09 kg/m³). To power a PEM (proton exchange membrane) hydrogen fuel cell vehicle with a 300 mile range, it is estimated that 5.6 kg of hydrogen would be needed onboard the vehicle [10, 14] translating into a need for 61.6 m³ of hydrogen onboard under STP conditions. Therefore, it is essential to increase the storage density of hydrogen for the purposes of powering light duty vehicles. In order to facilitate the increase in storage capacity, effective energy storage techniques are required capable of

meeting all of the Department of Energy targets for the development of hydrogen storage technologies [14,15] (DOE Targets can be found in Appendix A).

Several techniques exist for increasing hydrogen storage densities [16, 17]. Traditional storage has been achieved through the compression of gaseous hydrogen, while storage technologies in the literature include liquefied hydrogen storage and gaseous hydrogen that is stored via cryogenic compression or engineered storage materials.

Compression is currently the most widely used form of hydrogen storage though significant densities are not achievable for light duty vehicle applications. Storage systems of 35 MPa and 70 MPa have been evaluated in [18] and [19]. Even at 70 MPa, an energy density of only 4.4 MJ/L is possible [20]. Technical assessments [18] have shown that compressive systems do not meet the DOE density and cost targets and an alternative storage solution is required to develop an effective hydrogen storage system [19].

Cryogenically compressed hydrogen is an option that was developed as an alternative to liquid hydrogen storage at near ambient pressures [21]. These systems show an increased storage density over compressed gaseous hydrogen systems, though the systems have been shown to be too costly to be a viable option [21, 22]. Dynamic models of cryo-compressive storage showed that storage density was dependent upon initial tank temperature [23]. The study showed that with an initial tank temperature of less than 180 K, the theoretical storage density was found to be near 71 g-H₂/L (about that of liquid hydrogen). Cryo-compressed systems meet the volumetric goals though the manufacturing cost of developing a high compression cryogenic tank are too great [21].

Liquid hydrogen has been evaluated for onboard hydrogen storage because of its density, though significant issues with liquefaction and boil-off hinder its viability. In its liquid form, hydrogen has a density of 0.07099 g/cm³ (71 g-H₂/L), almost 800 times that of gaseous hydrogen. However, liquefaction of hydrogen is an energy intensive process. Over thirty percent of the energy stored in hydrogen is consumed during liquefaction [24, 25]; of the minimum work required (12,119 kJ/kg), only 8,343 kJ/kg is reversible work [25]. In addition to the high energy costs, liquid hydrogen storage tanks are highly expensive to limit heat transfer into the tank to control boil-off [15, 19]. Ultimately, liquid hydrogen provides high storage densities, though other storage techniques are pursued because of the costly and complex refueling systems and storing tanks [26].

Research has shown that hydrogen storage materials offer a possible solution to the hydrogen storage issues posed by the previously mentioned storage techniques because of their high storage densities at low pressures [15, 24], though they are more costly on a USD/kW-hr basis [27]. The most common materials present in the literature can be broken down into two categories: hydrides and adsorptive materials. Hydrides are materials that form physical and/or chemical bonds with gaseous hydrogen and show promise to be a viable solution for storage because of their high storage densities [28, 29]. Metal hydrides store hydrogen in interstitial sites within the material's lattice, while chemical hydrides react to create bonds with the hydrogen [19, 30]. In general, hydrides have higher storage densities than other materials because of the high packing density achieved by dissociating the H₂ molecules [31]. Storage densities of up to 170 g H₂/L (170 kg H₂/m³) are possible, which is more than double that of liquid hydrogen [24]. Examples of hydride materials are

Magnesium-based hydrides, which have demonstrated a 7.6 wt% reversible storage capacity [29, 30].

While hydrides have a high storage capacity compared to other storage media, releasing the hydrogen from these systems is a major drawback of chemical and metal hydrides [28, 31]. Hydrides are materials that typically have slow kinetics and release thermal energy during storage. To release hydrogen from the material, a significant amount of heat is required [24, 31]. Chemical hydrides are sometimes not reversible without a catalyst, in which chemical reactions are required in addition to the high temperatures and pressures needed to release the hydrogen [24, 28, 31]. Also, the catalyst systems require reconditioning to maintain acceptable storage densities [28, 31, 32].

Though hydrides have a higher storage density, adsorptive materials are a promising solution to the hydrogen storage challenge because of their reversibility, relatively high storage densities, fast kinetics and operation at lower pressures [19, 20, 33, 34]. A wide array of adsorptive materials have been developed and evaluated for hydrogen storage purposes [34, 35]. Adsorptive materials include carbon-based materials such as activated carbon [36], nanostructures [37, 38], and graphene [39]; metal organic frameworks (MOFs) [40, 41], covalent organic frameworks (COFs) [42, 43], and others [15, 33]. Adsorbents characteristically have a high surface area, in which temperature greatly affects the storage capacity [39, 44]. Because the hydrogen molecules are bonded to the surface by weak Van der Waals forces, the materials exhibit a very low storage density at room temperature, and capacities increase greatly with a decrease in temperature [26]. Theoretical maximum densities of undensified adsorbents were found to be 6.8 wt% at cryogenic temperatures and

pressures up to 50 atm [26, 45, 46]. Using various techniques such as compaction of the media, storage densities up to 8 wt% have been achieved under similar conditions [32, 39].

2.3 Microchannel Heat Exchangers for Adsorptive Storage

Hydrogen storage with adsorbents is greatly influenced by temperature. Optimal storage densities require temperatures below 100 K (cryogenic temperatures) at pressures up to 50 atm (5 MPa) [44, 47]. However, the adsorptive process is an exothermic reaction and the heat of adsorption is released when hydrogen bonds to the surface of the storage material. Heat released during adsorption must be effectively removed to maintain good storage conditions [31, 48]. Further, heat must be supplied to release hydrogen from adsorption beds. Though the thermal requirements of hydrogen storage via adsorptive media are well documented [31, 49, 50], there are no published solutions for managing the heat of adsorption for adsorptive materials.

Heat exchanging systems have been developed in the past few years though they were for use with metal hydrides and the systems occupy a large volume fraction of the storage system [51, 52]. Current heat exchangers include extruded aluminum fin and tube systems [51, 52], and spiral tube systems [53]. Fin and tube systems typically occupy up to 30% of the tank volume [51, 52]. Spiral tube systems have been developed that show a displacement volume of about 7% [52, 53] for managing temperatures within metal hydride beds. Though the spiral systems show the capability of managing the thermal effects of hydrogen storage, the small heat transfer surface area would not prove useful in systems where the media has poor thermal conductivity, such as adsorptive materials.

Consequently, a need exists to develop a highly effective thermal management system capable of enhancing storage densities while occupying a minimal displacement volume for adsorptive hydrogen storage. Microchannel process technology (MPT) has been used to accelerate the heat and mass transfer within heat exchangers leading to smaller form factors based on their high surface area to volume ratios and reduced diffusional distances [54]. Resultant microchannel heat exchangers show anywhere from a two to five times (or more) reduction over the size and weight for equivalent conventional heat exchangers [54]. It is expected that hydrogen storage heat exchangers with minimal displacement volumes could be developed at reasonable costs using MPT at high production volumes [55, 56].

In this research, a microchannel thermal management system is developed capable of managing the temperature within a hydrogen storage adsorption bed during adsorption. The design presented here enables the available adsorptive storage technologies to be usable in light duty vehicle applications. This work will build on prior results demonstrating the use of microchannel cooling plates for thermal management within adsorbent materials [57, 58]. In this paper, we demonstrate the ability to produce a thermal management system with minimal displacement volume that is capable of meeting many of the DOE goals being developed through the Hydrogen Storage Engineering Center of Excellence while using automotive manufacturing paradigms [57, 58]. Specific issues addressed within this paper are to demonstrate the ability to manifold cooling plates with adequate flow distribution between plates as well as the ability to withstand the thermal stresses that occur during cryogenic operation.

3. DESIGN

Figure 1 shows a concept for the Modular Adsorbent Tank Insert (MATI) investigated in this work. The MATI unit is a thermal management system designed to maximize the volumetric storage density of adsorbents by maintaining cryogenic temperatures within a cylindrical pressurized storage tank during tank filling. In the MATI unit, thermal and mass transport distances are minimized within the bed by separating the bed into a stack of modules separated by hydrogen distribution plates and cooling plates. At one end of the modules, chilled hydrogen is distributed radially from the exterior of the tank to the interior of the bed through the use of hydrogen distribution plates. The hydrogen is then transported axially within the bed where it is adsorbed. Because the temperature of the incoming hydrogen starts below the temperature of the bed, some of the heat of adsorption is removed during hydrogen adsorption. The remaining heat of adsorption is managed by liquid nitrogen cooling plates at the other side of each module. Liquid nitrogen is distributed to and from the cooling plates via header tubes located on opposite ends of the plates. The same cooling plate architecture can be used for desorption of the hydrogen during vehicle operation through the introduction of ambient air within the header tubes. As the cooling requirements for adsorption are much greater than the heating requirements for desorption, the architecture was designed to meet adsorption requirements. In addition, this cooling architecture was designed to be manufacturable; able to take advantage of the manufacturing capabilities used for producing automotive radiators.

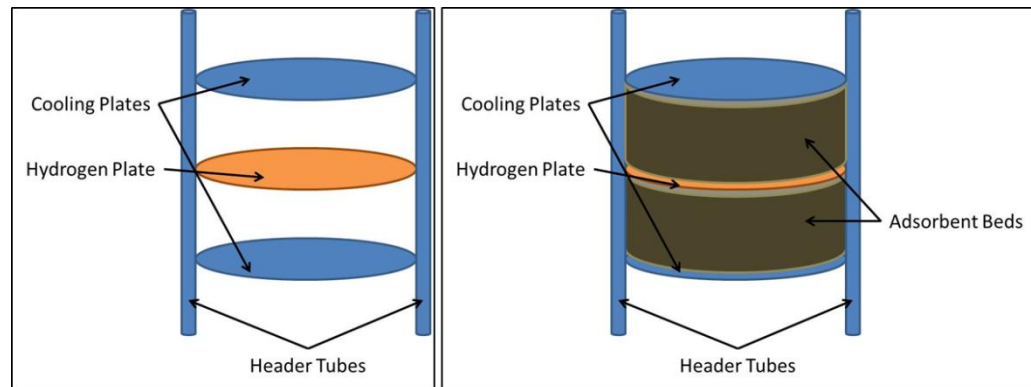


Figure 1: Geometric concept of the MATI for two adsorbent modules; without modules (left) and with modules (right)

Module height is an important geometric parameter within the MATI design. Too large of a module height and the bed will heat up leading to poor adsorption kinetics and heat transfer rates. Too small of a module height and the MATI unit becomes too heavy due to the increased number of cooling plates per unit volume. Further, the conductivity of the bed significantly influences the module height. As the thermal conductivity of the bed increases, the module height can be increased reducing the overall volumetric displacement and weight of the MATI. The MATI has been designed to manage the thermal effects at a heat of adsorption of 4 kJ/mol H_2 . Typical heats of adsorption for adsorbents are between 3-5 kJ/mol [39]. Figure 2 demonstrates the heat transfer requirements of the MATI. The designed modules take the form of short cylinders or disks with its diameter greater than its height.

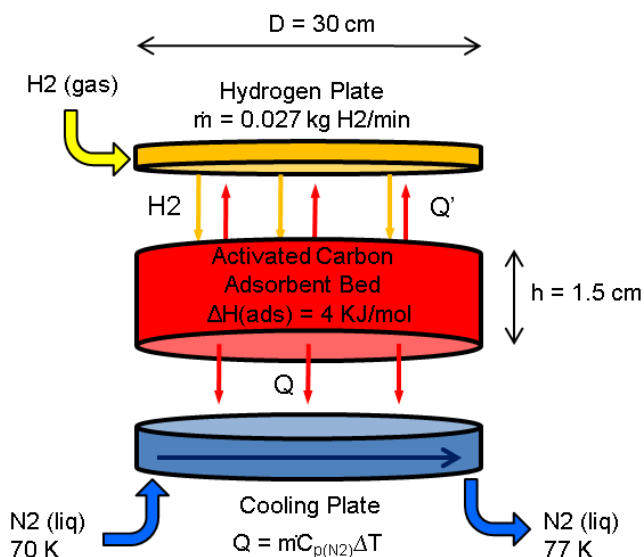


Figure 2: Heat exchanging functionality of the MATI with selected design specifications

One requirement of the MATI unit is to keep the liquid nitrogen from boiling during filling to avoid vapor lock and other issues associated with two phase flow. The boiling point for liquid nitrogen (LN_2) at one atmosphere is 77 K . Pressure drops were expected to stay below a few atmospheres. Further, the use of LN_2 cooling required that the system be hermetic, capable of withstanding the thermal stresses associated with operating in a cryogenic environment. Finally, the system was required to withstand up to 50 atm differential pressure, the assumed maximum storage pressure of the compacted adsorbent. Therefore, cooling plates were designed to withstand deflections which could pinch off flow or cause flow maldistribution across the cooling channels. A complete set of requirements is presented in Table 1.

As suggested above, key material requirements involved minimizing displacement volume (high strengths) and cost. In addition, the material was required to withstand the

stresses of the pressurized hydrogen while resisting hydrogen permeation, hydrogen embrittlement and the thermal stresses caused by cryogenic cooling. The high hydrogen pressures dictated the need for high elastic modulus materials to resist deflection. Further, the material needed to have a minimal coefficient of thermal expansion to minimize thermal stress during tank filling. The material also needed to resist potential erosion caused by high velocities in cooling plate inlets and outlets. Other requirements were based on the manufacturing and operational considerations of the MATI. Among manufacturing requirements, bonding and brazing techniques were required to achieve a hermetic joint at the interface of the cooling plates and header tubes.

Initial candidate materials were restricted to metals because of structural, thermal and manufacturing considerations. Metals that have been successfully used in hydrogen environments include pure aluminum; 6000 and 7000 series aluminum alloy; and 316, 22-13-5, A-286 and Fe-Ni-Co stainless steel alloys with a nickel content above 12% [59]. Aluminum and its 6000 and 7000 series alloys are a good selection for minimizing mass. However, as suggested above, displacement volume is a larger issue in adsorption beds than mass. Compounding this issue, the bonding and brazing of aluminum and its alloys is more difficult due to the thick native oxides on aluminum and its alloys. 316 stainless steel was selected to demonstrate the feasibility of a MATI unit due to its availability, machinability, joinability, high elastic modulus at room and cryogenic temperatures [60] and because it has been most commonly used in cryogenic systems [25] [60] and hydrogen environments [61-63].

Table 1: Design requirements

MATI Design Requirements	
Function	Remove heat of adsorption
	Provide heat for desorption
	Withstand 50 atm differential pressure
	Hermetically seal liquid nitrogen from hydrogen environment
	Introduce chilled hydrogen as a coolant halfway between cooling plates
	Allow hydrogen to access adsorbent axially
Material	Resist hydrogen permeation and embrittlement
	High modulus of elasticity at room and cryogenic temperatures
	Machinable (photochemical etching, milling)
	Joinable (diffusion bonding, welding, brazing)
	Low coefficient of thermal expansion

3.1 Modular Adsorbent Tank Insert Design

Three-dimensional CAD models, system models and detail design models were developed in parallel to visualize and evaluate design concepts. System analyses were evaluated based on the impact of design features on system displacement volume. System models were developed in Excel based on the design specifications used in the CAD models. Detail analyses were performed to investigate flow distribution, thermal distribution, pressure drop, and fin deflection within and between cooling plates. CAD models were developed using SolidWorks. Detail design analyses were performed on CAD models using computational fluid dynamics (CFD) and finite element analysis (FEA). A manufacturing plan was developed once a design was found to meet key requirements. The MATI unit was designed to be assembled using soldering/brazing baths commonly used in the automotive industry for the assembly of radiators. A detailed process-based cost model was then developed to estimate the cost-of-goods-sold of the proposed design.

The MATI was developed as a fin and tube type heat exchanger with three components: header tubes, cooling plates (LN2 plates) and distribution plates (H2 plates). A portion of the MATI system design is illustrated below in Figure 3, showing the thermal management system needed to manage the temperature within four modular beds. Each plate is assembled from two shims. The shape of each shim's periphery permits the header tubes to fit within the tank cylinder.

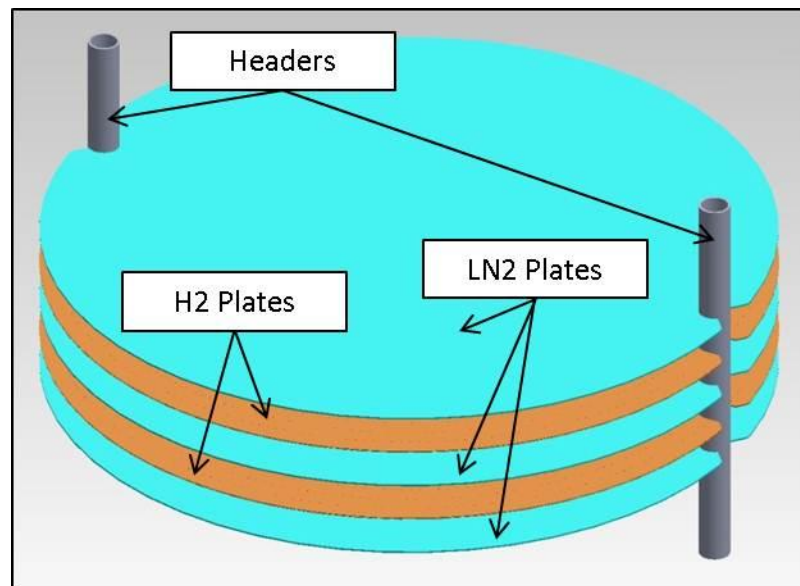


Figure 3: A partial MATI design for four adsorption modules (modules not shown)

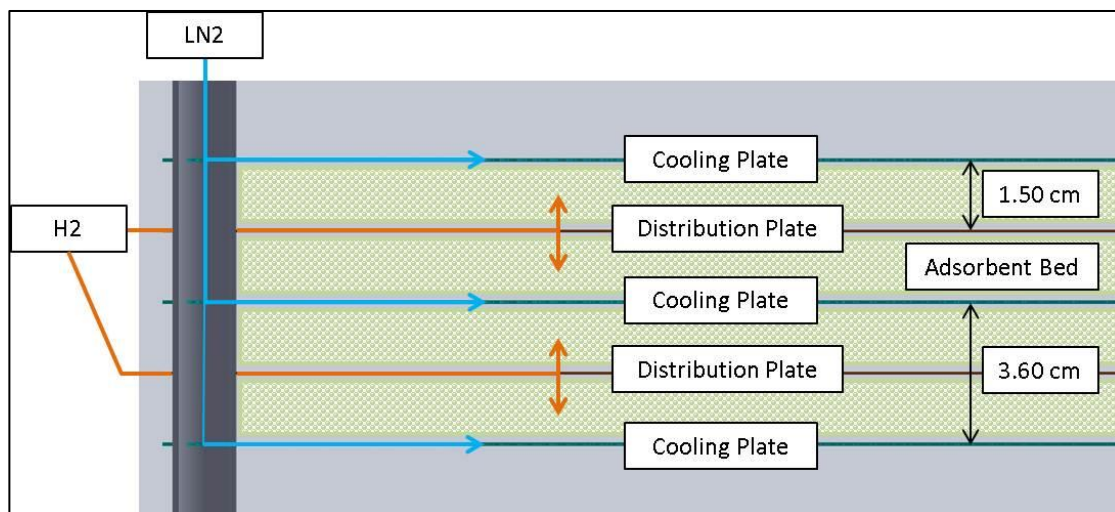


Figure 4: Fluid paths of the MATI; liquid nitrogen (cooling plate) and chilled hydrogen (distribution plate)

Each cooling plate was designed to remove the remaining heat of adsorption from the two adjacent adsorbent modules compensating for the cooling capacity of the chilled hydrogen injected through the hydrogen distribution plates (Figure 2, Figure 4). System models were developed to estimate nitrogen flow rate requirements based on the cooling capacity of the adsorbed hydrogen. The following assumptions (Table 2) were made in addition to those listed in Table 2.

Table 2: Assumptions for MATI system models

System Model Assumptions		
Adsorbent Density	560	kg/m ³
316 Stainless Steel Density	8000	kg/m ³
Hydrogen Storage Capacity	0.067	kg H ₂ /kg Adsorbent
Hydrogen Storage Requirement	5.6	kg H ₂
Fill Time	3.3	Min

The total heat flux generated by the adsorbent bed was found by calculating the total thermal load due to adsorption (78.5 kJ) during a fill time of 3.3 min (198 s) and was found to be 56.3 kW based on a heat of adsorption of 4 kJ/mol. It assumed that the connective heat transfer coefficient inside the microchannel device was at least as large as the conductive heat transfer coefficient within the adsorption bed. The heat transfer coefficient of the cooling plate was found to be 2478.6 W/m²-K with a Nusselt number of 8.24 (flow through parallel plates with a width to height ratio > 8 and constant heat flux) [64], a hydraulic diameter of 500 µm (5x10⁻⁴ m) and a thermal conductivity for liquid nitrogen of 0.1504 W/m-K at 70 K [65]. This shows that the cooling plate has the ability to easily remove the required heat due to adsorption. Under these assumptions, the cooling capacity of the incoming chilled hydrogen and the mass flow rates of the required liquid nitrogen were determined using the following basic equation:

$$\dot{Q} = \dot{m}C_p\Delta T \quad (1)$$

For the hydrogen flow, the average mass flow rate was found by dividing the total hydrogen mass required for the storage system (5.6 kg) by a fill time of 198 seconds as established in the 2017 DOE targets. The constant pressure heat capacity of hydrogen at 40 K was used for equilibrium para-ortho hydrogen with 85.12% para hydrogen (13,758.62 J/kg-K) [66]. Incoming hydrogen temperature is expected to be 40 K and the maximum allowable bed temperature of 80 K giving the incoming hydrogen a maximum temperature difference of 40 K. A temperature difference of 30 K was used to be more conservative in estimating the required liquid nitrogen flow rates. Consequently, it was found that 11.7 kW of the heat of adsorption could be removed from the incoming hydrogen. This suggested the need to

remove the remaining 44.6 kW of heat with liquid nitrogen. Liquid nitrogen flow rates were found to be 232 L/min based on a constant pressure heat capacity of nitrogen of 2042 J/kg-K at 70 K and an allowable temperature change of the liquid nitrogen of 7 K to avoid boiling in the cooling plate microchannels channels.

In prior work, efforts were made to analyze the modular bed height based on a tradeoff between the amount of adsorbent needed to store 5.6 kg of hydrogen (which increases with bed height due to higher temperature thermal profiles) and the displacement volume and mass of the thermal management system (which decreases with bed height due to fewer cooling plates) [57, 58]. A modular bed height of 1.5 cm was found to be suitable for the system configuration described above [67]. Therefore, each cooling plate was designed to remove the remaining heat of adsorption for two, 1.5 cm high beds after adjusting for the cooling capacity of the hydrogen.

Based on the constraints of the tank and detail analyses described in more detail below, key assumptions for system models regarding the geometry of the MATI unit are shown in Table 3.

Table 3: Geometric design specifications

Specification	Value			
Adsorbent Bed Diameter	0.3	m	=	30 cm
MATI Diameter	0.3	m	=	30 cm
H2 Top Shim Height	0.00025	m	=	250 μ m
H2 Etched Shim Height	0.00035	m	=	350 μ m
LN2 Top Shim Height	0.00025	m	=	250 μ m
LN2 Etched Shim Height	0.0005	m	=	500 μ m
Header Inner Diameter	0.030	m	=	30 mm
Header Outer Diameter	0.032	m	=	32 mm

Based on the hydrogen storage capacity for adsorbents given above, the final system configuration was found to consist of 142 modules of adsorbent including 71 hydrogen distribution plates and 72 cooling plates. Therefore, the cooling capacity requirement per cooling plate was to remove at least 620 W (310 W per cooling surface) at 3.2 L/min based on the heat flux of 4.4 kW/m² on each cooling surface. Final system mass and displacement volume for the MATI system are shown below.

Table 4: System model results for displacement volume

System Specifications		
Storage Tank Volume*	160.9	L
MATI Displacement Volume	10.1	L
MATI Volume Percent	6.3%	

*Storage tank volume is the minimum interior tank volume needed to enclose the MATI and the adsorbent beds

As shown in Table 3, the MATI occupies a displacement volume of less than 5%. This is over a 85% reduction in the percent displacement volume of the fin and tube type heat exchangers proposed by [51] and [52], and a 10% reduction in the percent displacement volume of the coiled tube exchangers proposed by [52] and [53] for metal hydride systems.

3.2 Detail Design

A manufacturing plan for producing the MATI was developed based on commonly used processing techniques for producing microchannel systems [54] and automotive

radiators. The cooling plates were designed to be photochemically etched from shim stock and were assembled together using diffusion bonding. Slots were machined into headers for assembly with cooling plates via brazing using a process similar to how headers on automotive radiators are joined to cooling fins and plates. The manufacturing plan is shown in Figure 5.

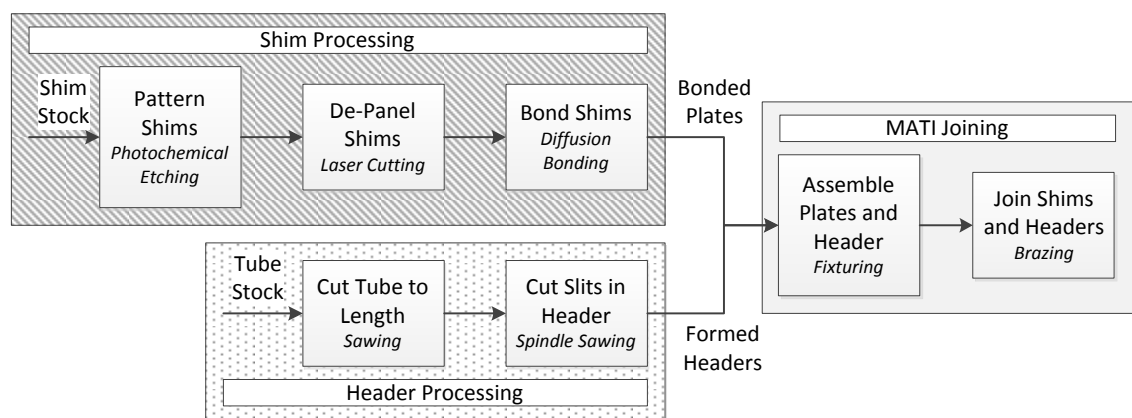


Figure 5: MATI Manufacturing Plan

The cooling plates (LN2 plates) are fluidic microchannel heat exchangers assembled from two shims. The blind-cut shim is photo-chemically etched to a depth of 250 μm in 500 μm thick shim stock. The top shim is a flat shim from 250 μm thick shim stock. The shims are joined by diffusion bonding to form a cooling plate (Figure 6).

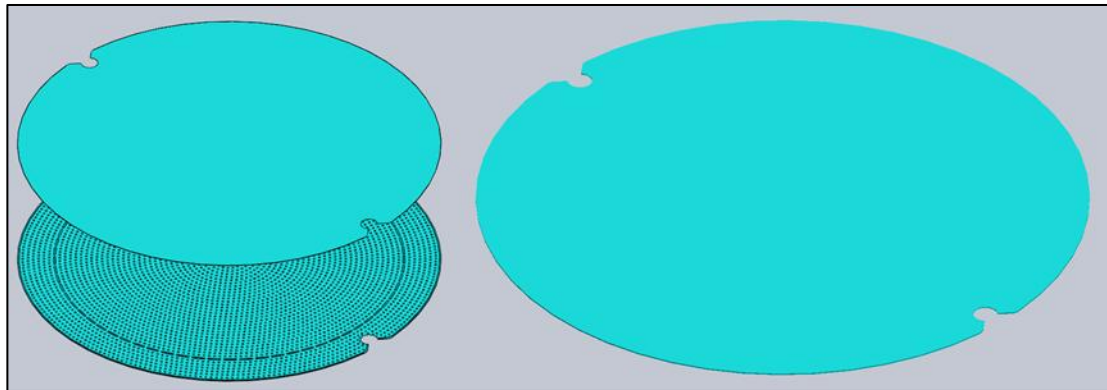


Figure 6: Patterned LN₂ shims (left) and bonded LN₂ plate (right)

Two rings are visible in the design of the etched shim. The outer ring is 500 μm wide and is used to hermetically seal the cooling plate along the edge of the shim during diffusion bonding. The inner ring was used to help distribute cooling fluid across the cooling plate. By having smaller hydraulic diameters through the inner ring compared to between the pillars, flow is partially redirected to the edges of the cooling plate.

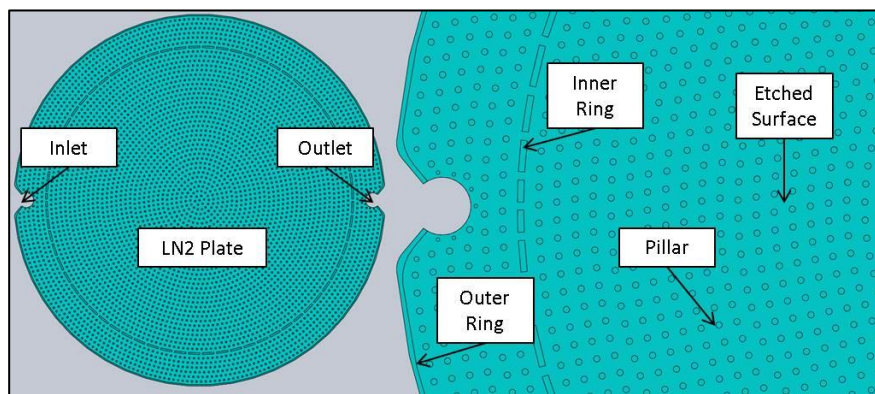


Figure 7: Top view of LN₂ etched shim to show pillar geometry, inlet, outlet and ring features

The inlet and outlet was shaped for good brazing fit-up and to allow the headers to fit within the periphery of the plates. Figure 8 shows the cross section of the header joint.

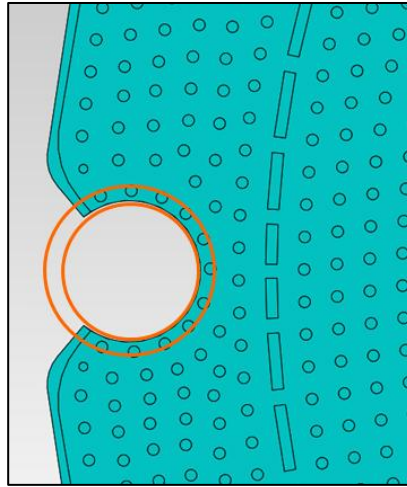


Figure 8: Top view of the cooling plate to show the cross section of the header at the inlet joint

The etched shims were designed having a network of pillars provide the structural support for the fluidic channel to withstand the differential pressures within the tank. Pillar diameters were selected to be 1.3 based on manufacturing requirements of PCM and to also serve as faying surfaces during bonding. The function of the pillars was to minimize deflection of the adjacent fins leading to increased pressure drop or flow maldistribution. Spacing of the pillars was selected based on Ansys FEA modeling of fin deflection caused by the differential pressure between the stored hydrogen and the liquid nitrogen. Initially, plate mechanics calculations showed expected deflections of $11.1 \mu\text{m}$ (4.4% average channel deflection) using Roarke's formula for deflection [68] of a circular disk with fixed edges and even pressure applied normal to the plate.

The FEA simulations were conducted on the three overlapping regions of the cooling plate to assess all possible pillar spans: the inlet, the center and an in-between section (Figure 10).

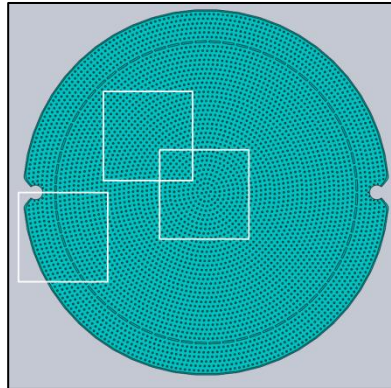


Figure 9: Regions of the cooling plate investigated by FEA

A symmetrical boundary condition was used for all outside edges and 50 atm uniform pressure was applied normal to all external surfaces. The symmetry boundary placed a frictionless support along the edges of the plates. The material properties used were for 316 stainless steel at 295 K (71 °F). The use of room temperature values provided a more conservative result since the strength of SS increases as temperature decreases. A rectangular polyhedron mesh was created and refined until no further change in deflection was found. The final mesh of the central section of the cooling plate is shown in Figure 10.

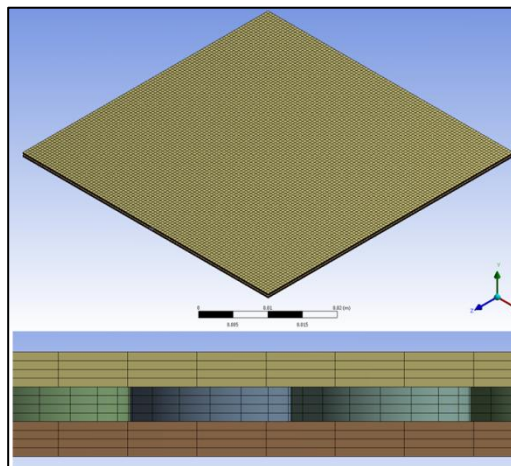


Figure 10: FEA mesh of the central cooling plate section

The pillar pattern was generated by specifying the distances between the adjacent pillars and the distance between each row of pillars. With a specified dimension of 3.5 mm between adjacent pillars and between each row, the largest span was found to be around 5 mm. The largest deflection was found in the center of the cooling plate, where the pillar spacing was found to be around 5 mm between the second and third row of pillars. The FEA results of the central cooling plate section can be seen in Figure 11.

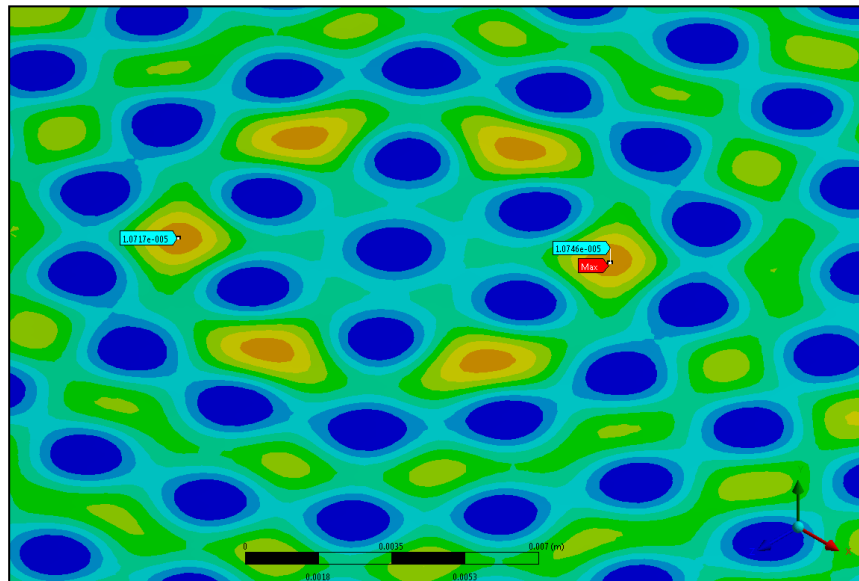


Figure 11: FEA deflection results of the central cooling plate section

Across the cooling plate, pillar spacing was found to be from 3.5 mm to 5 mm leading to a maximum deflection of 10.5 μm , which is equivalent to an average deflection of around 4% of the channel height across the pillar span. This suggests that the deflection due to the pressurized environment does not significantly affect the flow maldistribution across the plate.

The hydrogen distribution plates were similar in design to the liquid nitrogen plates but contained features to distribute the incoming hydrogen axially into the adsorbent beds. The etched shim of the hydrogen plate contains a blind cut etched channel with a depth of $100\text{ }\mu\text{m}$ from $350\text{ }\mu\text{m}$ thick shim stock (this maintains fin thickness of $250\text{ }\mu\text{m}$).

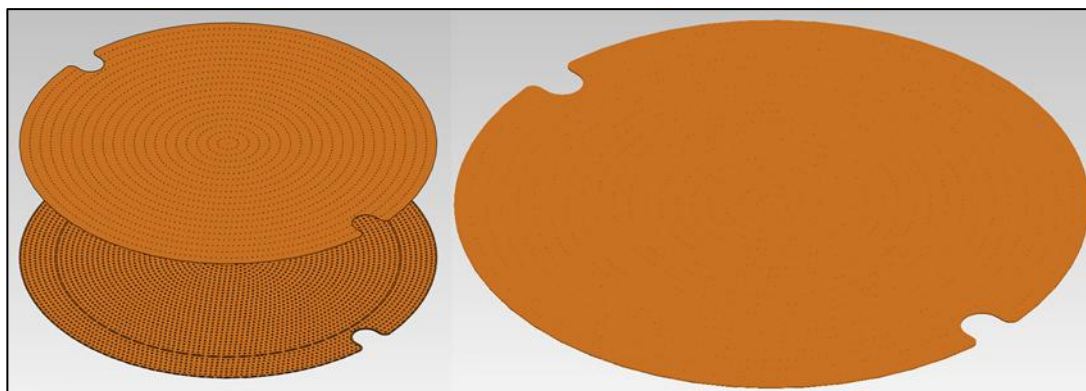


Figure 12: H2 shims (left) and bonded H2 plate (right)

The etched channel also features slits into several pillars to create a pathway to the though cut holes in the top plate that allow hydrogen to flow to the adsorbent beds (Figure 13). The top shim is a flat piece of shim stock with through cut etched holes. Through cut etched holes were obtained by applying etchant to both sides of the shim stock simultaneously. Another feature of the distributor plate that is different from the cooling plate is how the plates are joined to the header. The cooling plate is inserted into the headers to form a type of a lap joint, while the distributor plate forms a T joint (Figure 13) with the header tube because no LN2 fluidic interaction is required.

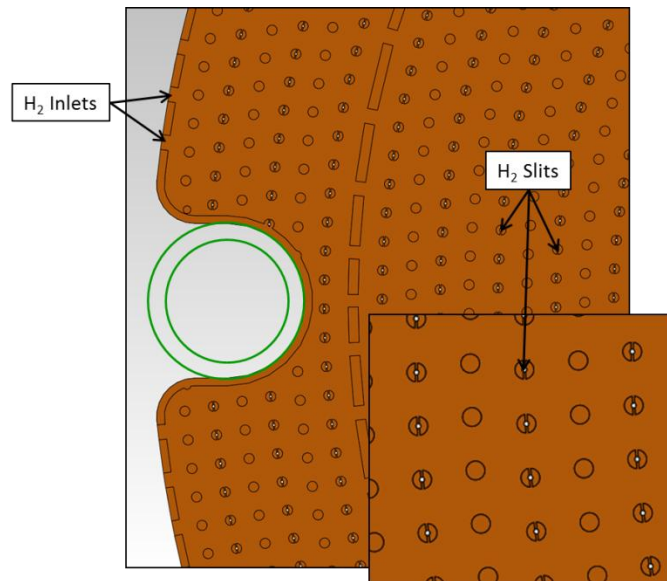


Figure 13: Top view of the H2 etched shim to highlight header joint and H2 pathways

The header tube was designed to ensure even flow distribution between cooling plates. The inner diameter was sized to keep the pressure drop through the header less than 10% of the pressure drop through a cooling plate. Header dimensions were determined by finding the pressure drop through the header using the flow rates required for the cooling plates. Once the flow rate was known, the Reynold's number was found at several points in the header. Pressure drop was then calculated for each section of the header with the header diameter that had a 10:1 pressure drop ratio versus the number of cooling plates fed by that header section. A weighted average was then taken of the header diameter for each point that was analyzed. The inner diameter was determined to be 20 mm with a wall thickness of 1 mm with this analysis. Further distribution analysis was conducted and is presented in section 3.3.2, showing that the header needs to have an inner diameter of 30 mm to ensure good distribution.

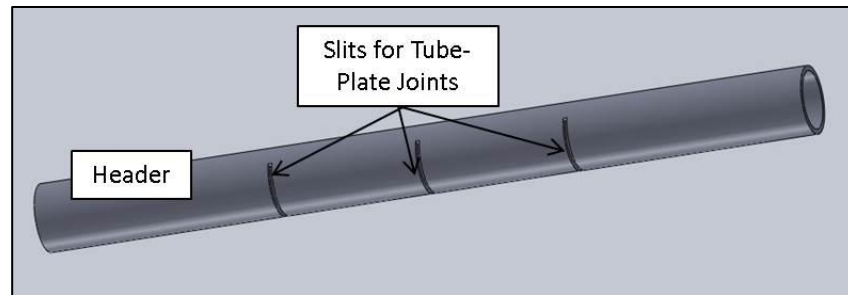


Figure 14: Header tube with slits for three cooling plates

It was determined that the cooling plates would be brazed to the header tubes in a manner similar to processes used to join automotive radiators. Joint cleanliness and fit-up are critical for designing a good braze joint [69]. Critical features for brazing need to have a clearance of less than 0.002 in (50 μm) for full joint penetration [69, 70]. The plate and tube joint was designed to have a clearance of less than 25 μm . The braze width is 1 mm due to the wall thickness of the header tube and the length of the braze joint is 110 mm long (perimeter of the inlet/outlet of the cooling plate). The design of the braze joint can be seen in Figure 8, Figure 13, and Figure 15.

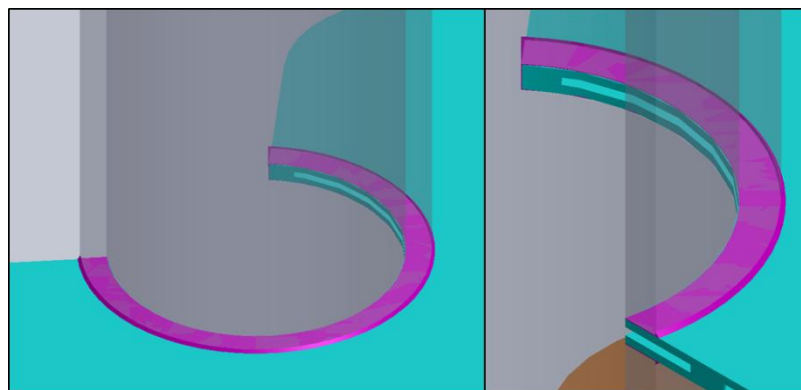


Figure 15: Header and cooling plate braze joint

3.3 Design Evaluation

The detail design of the MATI was evaluated based on key requirements and failure modes during operation. Key requirements included the cooling capacity, pressure drop, flow distribution and thermal distribution of the cooling plates. Key failure modes investigated were flow maldistribution between plates and thermal shock or thermal fatigue. Flow maldistribution between plates was controlled by header design. Thermal shock and fatigue were controlled by managing the thermal stresses associated with large temperature gradients, differential thermal expansion, or mechanical constraint. Because the requirements for the hydrogen distribution plates were less rigorous than those of the cooling plates, the focus of this investigation was the key functional requirements and failure modes of the cooling plates.

3.3.1 Flow and Thermal Distribution of a Single Cooling Plate

Thermal distribution is a critical feature in heat exchangers because hot spots can lead to degradation in heat exchange performance due to lateral heat transfer. Hot spots in the heat exchanger can further lead to boiling of the liquid nitrogen and vapor lock as well as hot spots in the adsorptive module and less stored hydrogen.

A CFD analysis was conducted using Fluent to evaluate the flow distribution at the flow rates (4.7 L/min per plate) and cooling capacities (656 W per plate) required to remove all of the heat of adsorption from two 1.5 cm high x 30 cm diameter modules with a single cooling plate. This level of heat removal represents a heat flux of 4.65 kW/m² for the cooling plate and is an overdesign by not accounting for the cooling capacity of the chilled hydrogen.

The model was used to evaluate the worst case for thermal distribution and pressure drop of LN_2 in the cooling plates.

CFD was conducted using a k-epsilon model with laminar, transitional, and turbulent flows. The simulation was first run as a laminar model to determine the initialization parameters for the laminar and turbulent model. A tetragonal mesh was used and refinement was conducted using the turbulent refinement algorithm in Fluent. The resultant mesh is shown in Figure 16.

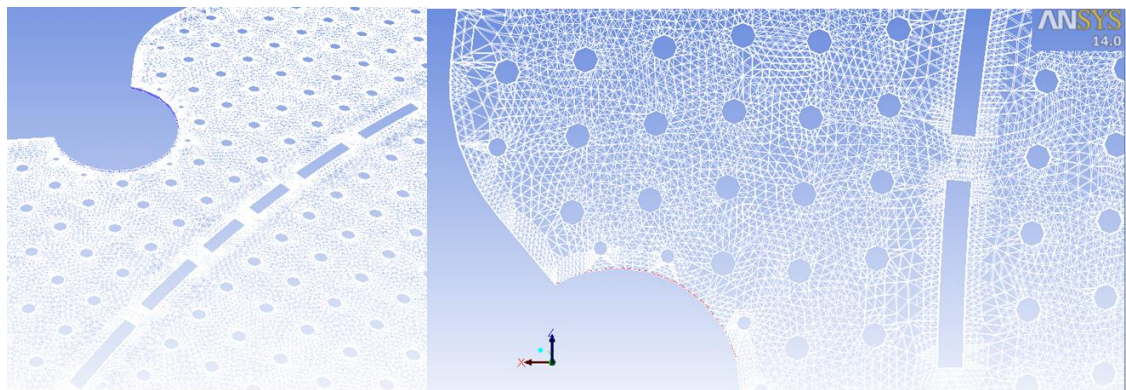


Figure 16: CFD mesh of the LN2 cooling plate inlet (courtesy of Daniel Peterson)

The Reynolds number at the inlet and outlet were found to be around 23,000 suggesting turbulent flow, though a Reynolds number of around 1000 was found across the majority of the plate suggesting laminar flow. Inlet velocity was found to be 9 m/s to generate a flow rate that would remove the heat of adsorption of two adjacent adsorbent beds without inducing boiling in the microchannels by limiting the delta T to 7 K.

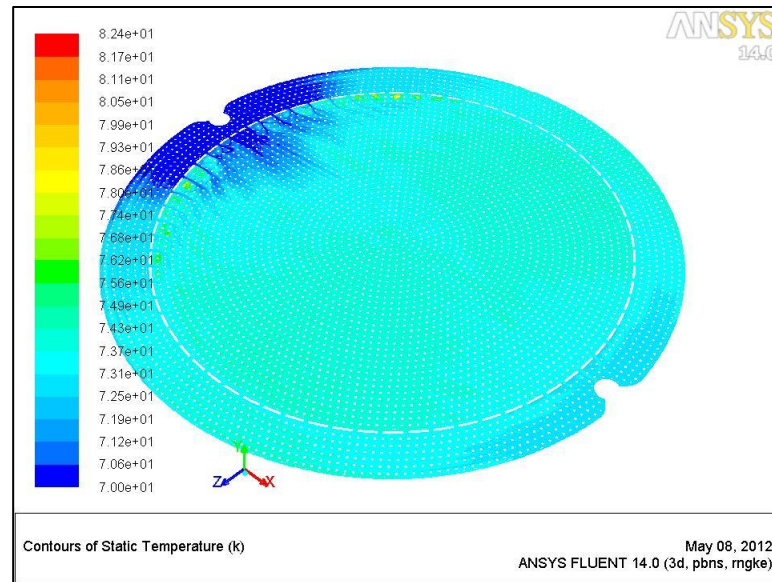


Figure 17: Temperature profile of the LN2 plate from CFD simulation (courtesy of Daniel Peterson)

Figure 17 shows a steady-state solution of the thermal profile for liquid nitrogen in the cooling plate that occurs during hydrogen storage. The simulation investigates the thermal effects of hydrogen storage and shows how the cooling fluid removes the heat of adsorption. The thermal profile shows that the cooling fluid flow is evenly distributed across the plate. Also, Figure 17 shows that the thermal gradient from the inlet to the outlet is 7 K across the cooling plate, indicating that boiling in the microchannel is not an issue. The pressure drop was found to be 336 kPa (3.32 atm, 48.81 psi) across the cooling plate, with the majority of the pressure drop occurring at the inlet and outlet. These pressure drops were found to be reasonable on an automotive platform.

Further CFD investigations showed that by considering the H_2 cooling, the pressure drop was reduced to 245 kPa (2.4 atm, 35.5 psi) with a temperature difference of less than 7 K using a flow rate of 3.2 L/min and an inlet velocity of 6.2 m/s. The liquid nitrogen velocities

at the inlet and outlet are high enough to potentially cause erosion of the stainless steel material. It is expected that the LN₂ will be delivered without significant particulate matter so that erosion issues are minimized.

3.3.2 Flow Distribution of Multiple Cooling Plates

Upon completing the cooling plate CFD, a flow distribution model was developed in excel to simulate how well the flow is distributed through the system. Header sizing is the critical design parameter to ensure proper flow distribution between plates. A model was developed in excel to calculate the flow distribution between a certain number of plates based on the pressure drop ratios between the cooling plates and the header tubes.

Table 5: Excel model to calculate flow distribution between the cooling plates (courtesy of Daniel Peterson)

Node Location		
Plate #		
Inlet		Outlet
1		146
2	P1	145
3	P2	144
4	P3	143
...	P...	...
72	P71	75
73	P72	74

The model presented in Table 5 used pressure drop calculations based on the Reynold's number found at each joint (node location) due to the flow rates required to distribute fluid to and from all subsequent cooling plates. Initially, flow was assumed evenly distributed through all plates. By calculating the relative pressure drop through each flow path, the flow non-uniformity was found. First, the pressure drop was calculated through

the inlet header at based on the flow rate through each node. The model then incorporated the pressure drop obtained through CFD across each cooling plate and calculated the pressure drop of the outlet header with the flow rate at each outlet node. A non-uniformity percentage was then obtained by finding the relative resistance to flow (R^*) of each flow path based on the assumption that resistance to flow was relative to the square root of the pressure drop through a given flow path (Table 6). The middle values are closer to zero because the non-uniformity was with respect to the pressure drop of the flow paths through plates 45 and 46. Flow non-uniformity is greatest farthest from the inlet due to the pressure drop of the entire tube length.

Table 6: Multi-plate flow distribution results (courtesy of Daniel Peterson)

Plate	R^*	Flow Non-Uniformity
P72	608.8	3.55%
P71	607.6	3.36%
P70	606.5	3.17%
P69	605.5	2.99%
P68	604.4	2.82%
...
P48	589.1	0.21%
P47	588.6	0.12%
P46	588.1	0.03%
P45	587.6	0.05%
P44	587.2	0.13%
P43	586.7	0.20%
...
P5	580.5	1.27%
P4	580.5	1.27%
P3	580.5	1.27%
P2	580.5	1.27%
P1	580.5	1.27%

It was shown that with an inner diameter of 30 mm, a flow non-uniformity of less than 5% could be attained across all 72 cooling plates. Previously, 5% flow variation was determined as the tolerance at which heat exchanger effectiveness significantly decrease [54].

3.3.3 Thermal Effects

The cryogenic environment has potential to cause mechanical failure because of three thermal failure modes. First, because of the large temperature range the storage tank will operate in, thermal gradients are of major concern. It is assumed that the maximum internal tank temperature will be 160 K. At the start of tank filling, a thermal gradient of up to 90 K can be seen across the fins and the braze joint because LN2 enters the system at 70 K. However, the greatest thermal stress will be when that gradient is applied across dissimilar materials causing differential thermal expansion such as at the braze joint. Third, as the liquid nitrogen begins to enter the upper plates within the thermal management system, contraction of the top plate can lead to mechanical strains for lower plates. Here, thermal modeling constraints limited the thermal system evaluation to experimental testing. Results are presented in section 5.2.

3.4 Cost Model

A cost model was developed for the MATI based on the manufacturing plan developed above. The cost model is a process-based bottom-up model developed in Excel similar to the models used in [56] and [55]. The model takes into account raw material, capital equipment, equipment maintenance, capital facilities, labor, consumables and utilities for each process step. Vendor quotes were used as the basis of capital equipment

amortization. Facilities amortization was based on unit area costs used in the construction industry times twice the equipment footprint. Labor, maintenance, consumables and utilities were based on equipment vendor interactions and specifications. Equipment capacities were determined based on three shifts over 360 days and estimates were made for yield, utilization and throughput based on process experience at the Microproducts Breakthrough Institute (MBI). The process steps included in the model were:

1. Cleaning, PCM, laser cutting and diffusion bonding of the shims;
2. Cutting and sawing of the tubes; and
3. Fixturing and brazing to assemble the MATI

Figure 18 shows the impact of production volume on the cost of goods sold for one MATI. The model was developed with the assumption that the diffusion bonding cycle could bond 42 panel stacks per cycle. Each panel stack (two pieces of shim stock) is a set of panels that will be singulated into 16 cooling plates after bonding. Therefore, 672 cooling plates were bonded per hot press cycle. The number of panels bonded per cycle was determined assuming a 12" high work zone with a 0.25" platen between each panel stack.

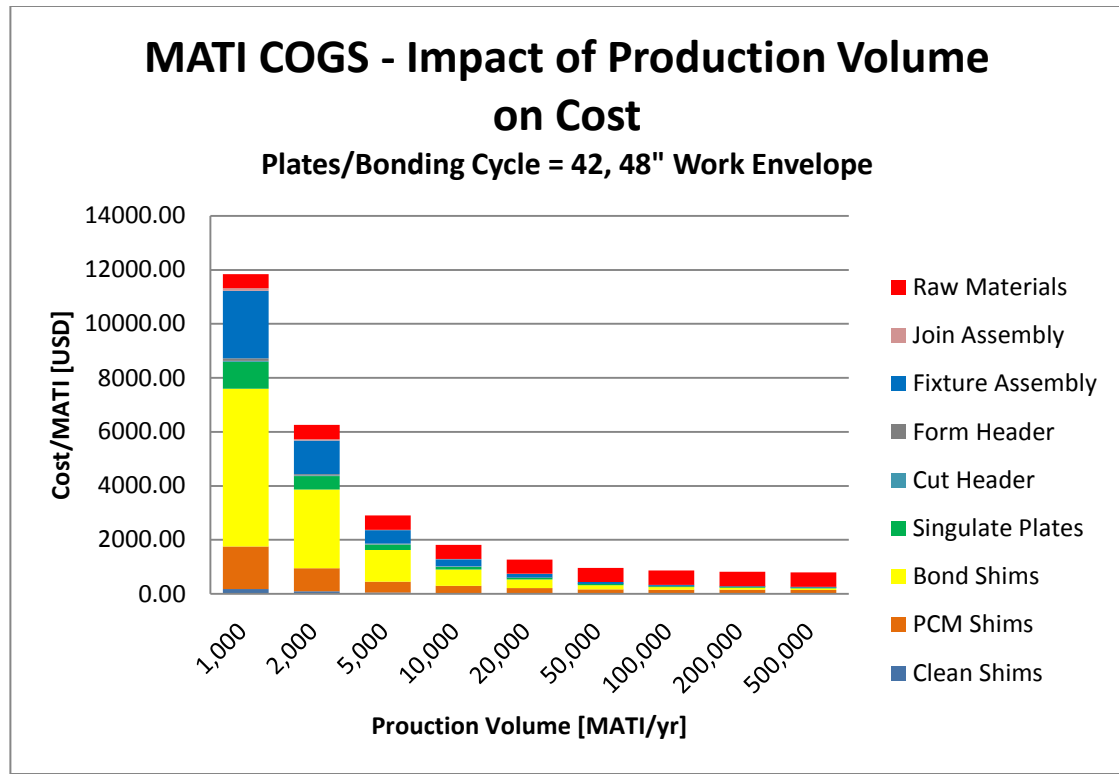


Figure 18: MATI COGS for 42 plates per bonding cycle at various production volumes

As shown in the graph above, a knee in the curve can be seen around 50,000 MATIs per year. This shows that beyond a production volume of 50,000 MATIs/yr, the cost per MATI will not decrease significantly. At 500,000 MATIs per year, the COGS have been estimated at \$788.92 based on the assumptions made in the model.

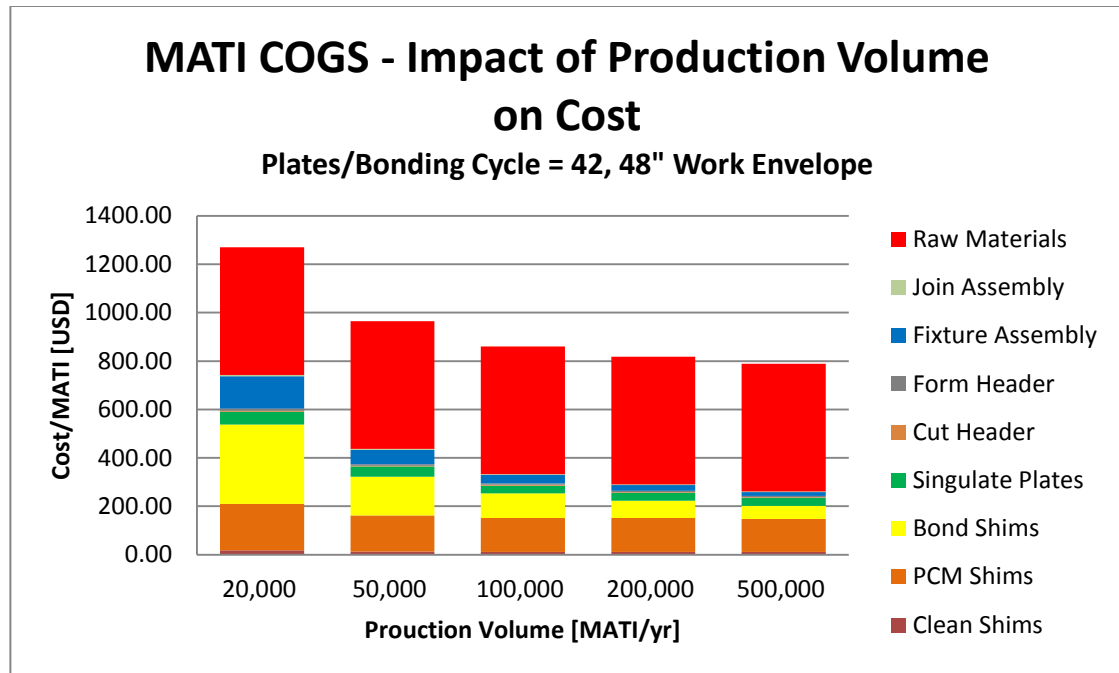


Figure 19: MATI COGS at high production volumes to show major cost drivers

At high production volumes (Figure 19: MATI COGS at high production volumes to show major cost drivers), the major cost drivers can be seen. As is typical in high production values of microchannel systems [55] [56], raw materials is the major cost driver. Forming the shims using PCM is the second most significant cost driver due to the fixed cost per m² for consumables such as the etch photomask and etch regenerates. The diffusion bonding cycle is the third most significant cost driver. By selecting a less expensive material and selecting a more economical forming and bonding operation, cost could significantly be reduced (Appendix A).

The following waterfall chart shows the impact of work envelope and the ganging of panel stacks during diffusion bonding. The chart illustrates how processing conditions greatly affect the cost of goods sold (COGS) of the MATI.

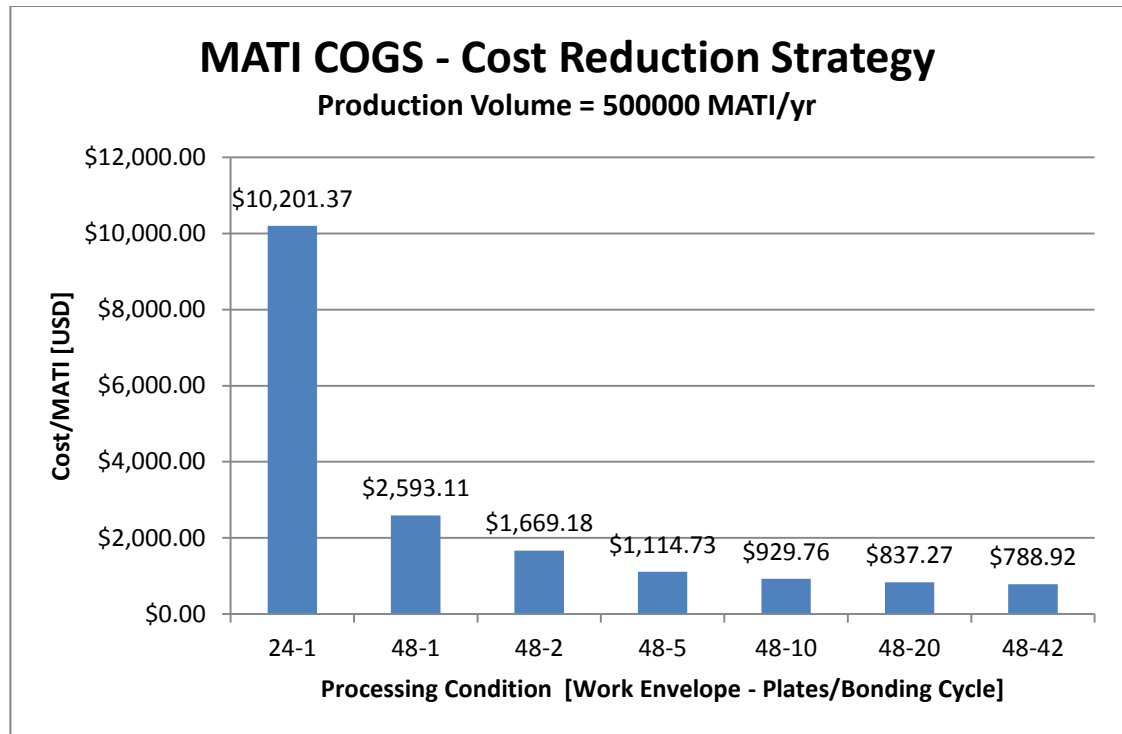


Figure 20: MATI COGS due to processing parameters

The left most column (24-1) shows the cost to develop a MATI using a 24" work envelope (24" x 24" work space) while one panel stack (two pieces of shim stock) is bonded at a time. The cost is so great due to poor materials utilization. The second column (48-1) shows the impact of changing to a 48" work envelope. By adjusting the work envelope, 16 shims were able to fit on each piece of shim stock, greatly increasing materials and tool utilization. Subsequent columns show the impact that ganging in the diffusion bonding cycle has on the COGS. The second number on the label (-X) indicates the number of plates that are bonded per diffusion bonding cycle. The column title 48-42 is representative of the maximum number of plates that can be bonded at once within a 12" high hot zone, including 0.25" platens between each shim stock set to ensure the stress is delivered evenly through

the bonding stack. The decrease in cost due to gang pressing diminishes as the number of plates per cycle increases because diffusion bonding becomes less of a cost driver. With few plates per cycle at low production volumes, the high capital cost and the long cycle time of the vacuum hot press significantly affects the COGS. Figure 18 shows that the contribution of diffusion bonding diminishes with higher production volumes. At high volumes, raw material costs dominate, while PCM is the largest process cost driver due to the fact that acid regeneration and photoresists are insensitive to production volumes.

4. EXPERIMENTAL APPROACH

To validate the above design, several sub-scale prototypes were fabricated to evaluate some of the key functionality and to investigate key potential failure modes of the MATI design. Two experiments were conducted on sub-scale prototypes as shown below:

1. Fluidic system evaluation (functional requirements)
 - a. Flow distribution across a cooling plate;
 - b. Flow distribution between multiple cooling plates;
 - c. Cooling capacity; and
 - d. Pressure drop through the multiple plates
2. Thermal stress evaluation (key potential failure mode)
 - a. Thermal shock due to
 - i. Thermal gradients;
 - ii. Differential thermal expansion/contraction of the braze joint; and
 - iii. Failure due to mechanical constraint
 - b. Thermal fatigue over 10 cycles

4.1 Prototype Design and Fabrication

Three sub-scale MATI prototypes were fabricated for experimental validation and to evaluate the manufacturability of the design and proposed manufacturing processes. The three 5 cm diameter cooling plates were designed to remove at least 52 W (4.4 kW/m² per

cooling surface \times 2 surfaces per plate \times 3 plates) of heat at a water flow rate of 149 mL/min, an inlet temperature of 291 K and an outlet temperature of 296 K. The hydrogen plates were not included in the fabrication because the experiments were designed to evaluate the operational performance of the hermetic fluid network.

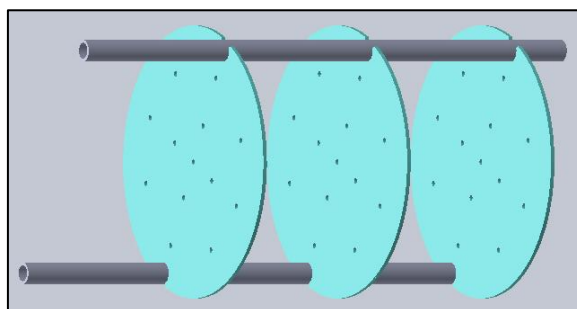


Figure 21: Design of the MATI prototype with three cooling plates and header tubes

The prototype was fabricated using the same manufacturing plan established for the full-scale MATI (Figure 5) to assess manufacturability. The design of the plates and headers were similar to the full-scale models to closely assess the functionality of the full-scale model. A difference that is present in the prototype is the inclusion of through holes in the liquid nitrogen plates. These holes were designed as thermocouple ports in case the plates were used to experiment with adsorbents.

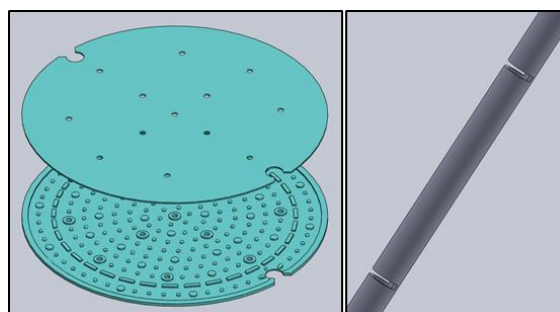


Figure 22: Design of the top shim and etched shim of the LN2 Plate (left), and design of the header tube (right)

Cooling plate shims were photochemically machined (PCM) to a depth of 250 μm from 500 μm thick sheet stock to create the fluidic channel. Through holes were etched by PCM on both sides of the shims. The perimeter of the top shim and the etched shim were laser cut.

Prior to fabrication, the shims were characterized for etch depth. An optical profilometer was used to verify the etch depth. Ten samples were taken from 5 different cooling plate shims. Average etch depth was found to be 261.3 μm with a standard deviation of 9.1 μm which at a 95% confidence interval is an etch variation of 6.9% (Appendix C). Based on prior work, etch depth tolerances below 5% are desired across the plate to minimize the effects of flow maldistribution in and between the plates on heat exchanger effectiveness [54].

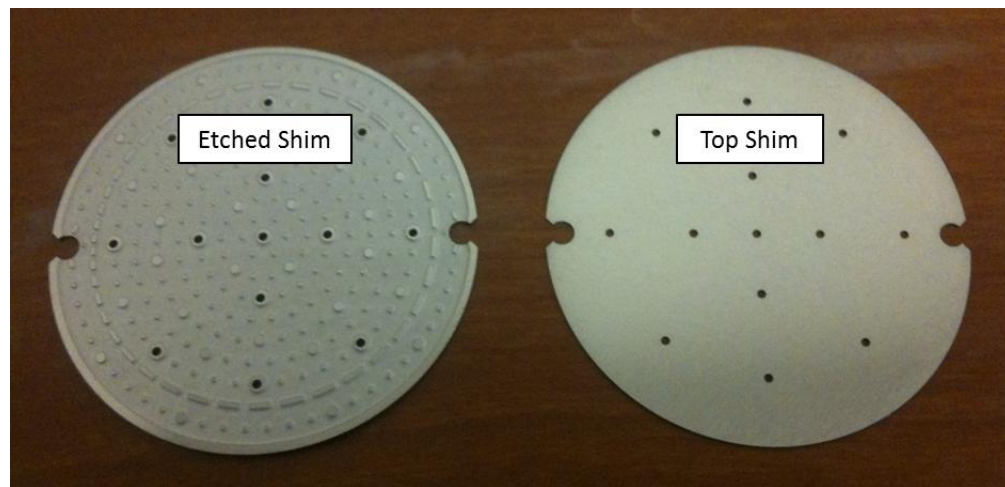


Figure 23: Fabricated LN2 shims (PCM and laser cut)

The shims were diffusion bonded using a vacuum hot press. Critical parameters of diffusion bonding are time, temperature, pressure and atmosphere. The shims were bonded

at 975 °C for 180 min with 1000 lbf at atmospheric pressures below 5×10^{-5} torr. Fixturing was made from graphite and plates were gang pressed to bond three cooling plates in one bonding cycle. Fifteen cooling plates were bonded with a 100% yield based on hermeticity testing described below. All shims were visually inspected with an optical microscope to verify the bond along the outer faying surfaces of the shims. Pressure uniformity on the shims appeared to be excellent based on the parallelism of the graphite brazing platens and ram used during the hot pressing cycle. Each platen was machined to have a parallelism of less than 0.0005 in (12.7 μm). The cooling plates were found to have a parallelism of around 13 μm after bonding. Out-of-parallelism was mainly due to creep of the top plate over unsupported regions during diffusion bonding.

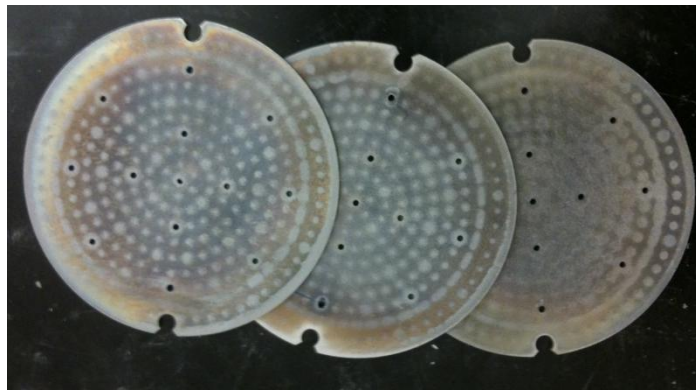


Figure 24: Bonded LN2 plates

The header tube was made from rolled 316 stainless steel tubing and had a 3 mm inner diameter with a 0.5 mm wall thickness. Tubes were machined using a vertical end mill and fixturing was designed to enable the fabrication of the tubes without structural failure due to the cutting forces. The fixture allowed for the tube to be clamped in place for the first cut then rotated to make the second cut, forming the faying surfaces of the tube.



Figure 25: Tube machining fixture; setup on a vertical milling machine (top), fixture and clamps (bottom)

The slits were designed so that a first cut would cut half-way through the tube, the fixture would rotate 45° and then a second cut would be made half-way through the tube. The result is a slit where, in cross section, 75% of the tube section is removed to fit up with the cooling plates. The shape of the cut only allowed the tubes to be fit onto the plates in one direction so assembly errors due to misplacement of the header were eliminated. Tube slits were required to be $750\text{ }\mu\text{m}$ high plus a $25\text{ }\mu\text{m}$ clearance for brazing joint fit-up. A 0.03" ($762\text{ }\mu\text{m}$) wide end mill was used to cut the slits. Slit width was measured using an optical microscope. An average slit width of $767.7\text{ }\mu\text{m}$ was produced with a standard deviation of $5.9\text{ }\mu\text{m}$ for 18 slits.

The prototypes were joined using Braze 820 (BNi-2), a nickel based braze material supplied from Lucas Milhaupt. Critical parameters for brazing were temperature hold time, vacuum, joint fit-up and joint cleanliness. The shims were prepared and cleaned with

deionized water, acetone, methanol and deionized water wash prior to brazing. The brazing cycle followed the temperature profile in Figure 26 using a CamCo J-12 Combo Furnace.

Table 7: Vacuum brazing cycle

Time Step	Duration [min]	Temp [C]	Details
0	0	16	Initial
1	20	16	Purge to Vacuum
2	20	700	Ramp
3	5	700	Hold
4	5	900	Ramp
5	5	900	Hold
6	5	1100	Ramp
7	5	1100	Hold
8	-	100	Partial Pressure Fill
9	-	20	Cool Down

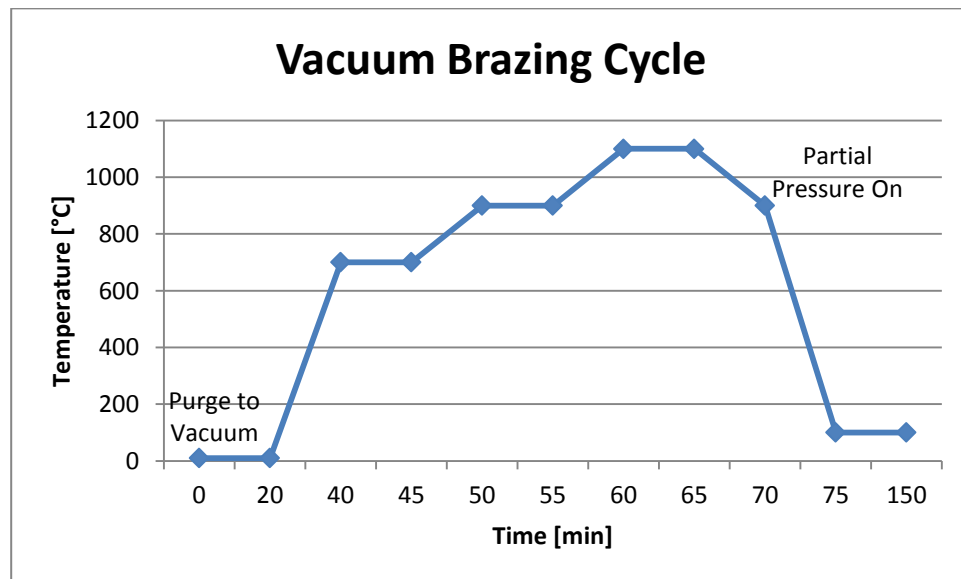


Figure 26: Vacuum brazing temperature profile

Initial brazing results were assessed using 100 psia air by leak testing the prototypes in water. Bubbles indicated any issues with hermeticity. The leak testing was used to evaluate both the bonding and brazing cycles. Two of the three prototypes were leak proof and one had a minor leak in one braze joint which was subsequently repaired by running a second cycle. In total, 17 of 18 braze joints were hermetic which is a 94.4% braze joint yield and a 67% device yield.



Figure 27: Fabricated MATI Prototypes

Upon completing fabrication, experimental test loops were set up for both prototypes. Thermocouples were calibrated using digital thermometers attached to a heat source, pressure sensors were calibrated with an Omega DPG400 pressure gauge, the Malema M-1500 mass flow meter was calibrated by catching and weighing the water over a specified amount of time, and the power supply to the heaters was calibrated with a digital multimeter. Thermocouples were evaluated at room temperature to show no deviation from the specified error of ± 0.2 °K.

4.2 Fluidic System Evaluation

The fluidic system evaluation investigated the flow distribution characteristics of the MATI prototype using water as the working fluid. Four criteria were used to assess the functionality of the MATI system design:

1. Cooling capacity;
2. Flow distribution across a cooling plate;
3. Flow distribution between multiple cooling plates; and
4. Pressure drop through the system

The experimental setup to assess these functional criteria is shown in Figure 29. The block diagram shown below is representative of the experimental setup.

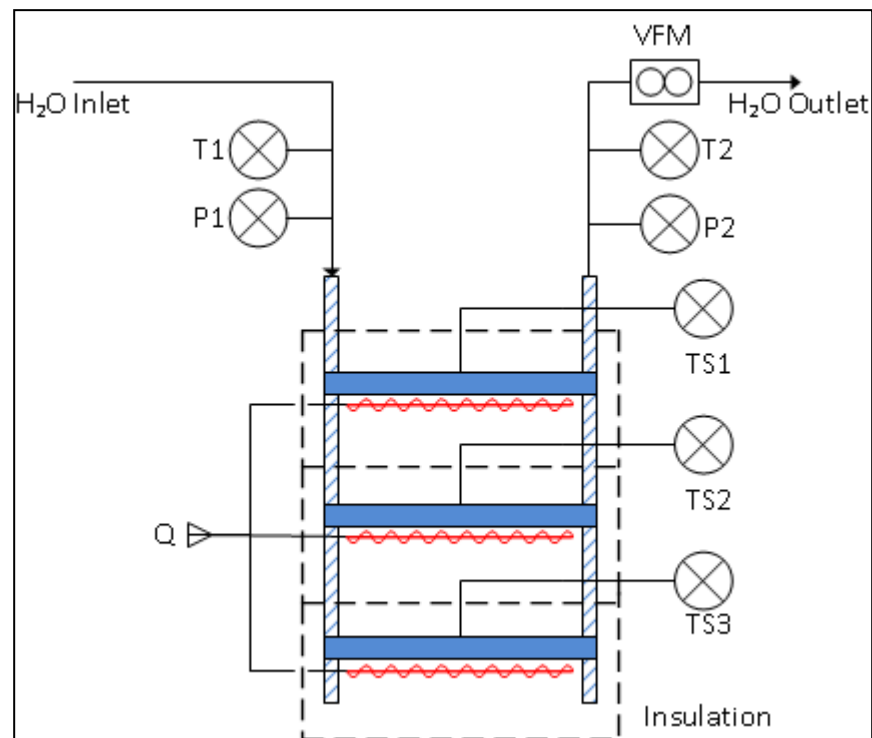


Figure 28: Block diagram of the fluidic system evaluation

The thermocouples outside of the insulation are for determining the thermal gradient of the system when a known heat load is applied. The pressure transducers show the differential pressure of the cooling fluid. The thermocouple sets on the top surface of the cooling plates are to show the thermal distribution and the resistive heaters on the bottom of the cooling plates supply the heat load.

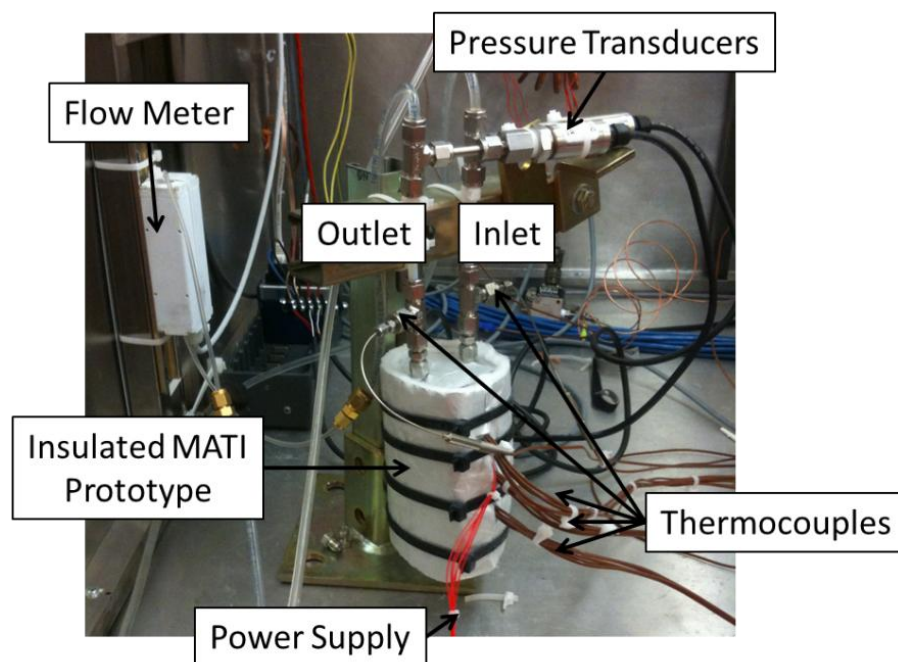


Figure 29: Experimental setup for fluidic system evaluation

Cooling capacity was evaluated by applying 17.33 W per heater (from two cooling surfaces at 4.4 kW/m^2) for a total heat load of 52 W across the three resistive heaters (Figure 31) and running the water mass flow rate through a range of values. The temperature difference from the inlet and the outlet was measured and compared with calculations based on Equation 1. It was calculated that 149 mL/min would remove the

applied heat load using the density of water at 1000 kg/m^3 and a constant heat capacity of 4185.5 J/kg-K .

At the same time, flow distribution was evaluated during the cooling capacity tests. Thermal profiles were logged and charted from the top of each cooling plate (Figure 30). The data was collected and compared across each cooling plate as well as between the cooling plates. The temperature profiles across each plate indicate the flow distribution for each plate, while temperature profiles between plates indicate flow distribution of the headers to and from each cooling plate.

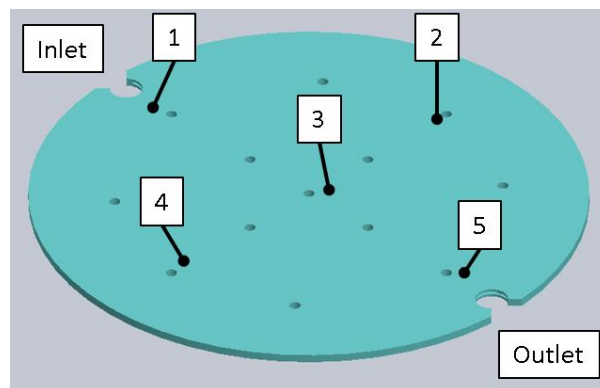


Figure 30: Thermocouple placement for thermal distribution tests (on top side of cooling plate)

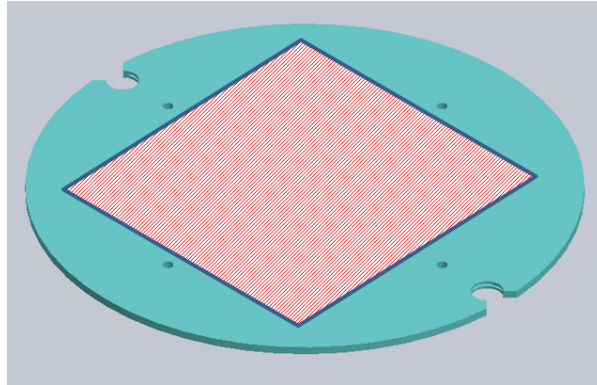


Figure 31: Resistive heater placement for cooling capacity and thermal distribution tests (on bottom side of the cooling plate)

Pressure drop was evaluated using pressure transducers connected to the inlet and the outlet of the prototype test loop. Pressure was instantaneously measured and the data was plotted against flow rate. The pressure drop of the MATI prototype was found by subtracting the total pressure found for the MATI by the pressure drop obtained by connecting a bent tube in place of the MATI. The experimental pressure drop was used to validate the CFD model of the MATI prototype.

4.3 Thermal Effects Evaluation

The second experiment was designed to assess the effect of thermal stress on the prototypes. Each joint was visually inspected and tested for leaks according to AWS C3.3:2002 [69] prior to the experiments. The MATI was then subjected to a worst case scenario thermal stress test, where two thermal shock and thermal cycling failure modes were evaluated caused by any one of the following:

1. Thermal gradients;
2. Differential thermal expansion/contraction of the braze joint; and
3. Failure due to mechanical constraint.

The largest thermal gradient expected in the storage tank is 90 K, from the temperature before fill (160 K) down to the temperature of the incoming liquid nitrogen (70 K). However, to be conservative, the MATI prototypes were exposed to liquid nitrogen from room temperature (294 K). The integrity of the joints was evaluated by the hermeticity of the joints either during or after testing. Two methods were used to evaluate the mechanical integrity of the joints due to thermal shock and thermal fatigue as described below.

First, to assess thermal shock effects, a Dewar was filled with liquid nitrogen and the prototypes were subjected to ten controlled dunks in which the prototypes were submerged one cooling plate at a time. Each cooling plate was held submerged for 5 seconds before moving to the next cooling plate. This evaluated not only the effect of large thermal gradients and differential thermal expansion across the braze joints; it also evaluated the effect of mechanical constraint from one cooling plate to the next. Once the prototype was fully submerged, it was held below the surface for 30 seconds before being removed and left to air dry. Dunk tests were performed 10 times in order to assess thermal cycling effects. Leak tests were conducted after each dunk by plugging the outlet and pressurizing the MATI prototype with air at 100 psi while submersing the prototypes in water to check for bubbles.

A second set of experiments were conducted to provide a more realistic assessment of thermal stress buildup within the MATI unit. This test was performed by connecting the MATI unit to a LN2 test setup and flowing LN2 through the system until the channels reached temperatures below 80 K. Leak testing was used after the test to assess the impact on hermeticity.

5. EXPERIMENTAL RESULTS

5.1 Fluidic System Evaluation

A CFD simulation was conducted to establish the expected results of the experiments. The results showed that a pressure drop was expected to be 1.01 psi at a flow rate of 149 mL/min with the addition of the pressure drop calculated through the headers on the MATI prototype. A heat load of 17.3 W was applied to the cooling plate (4.4 kW/m^2 per surface). Figure 32 shows the thermal distribution of the cooling fluid in the cooling channel and also shows the inlet and outlet temperatures for the cooling capacity calculations. The thermal gradient was expected to be linear from 291 K at the inlet and 296 at the outlet, showing a temperature gradient of 5 K. The thermocouples perpendicular to the flow direction was expected to be uniform at 293.6 K. Probed points at the specified points were used to compare against the experimental results for thermal distribution.

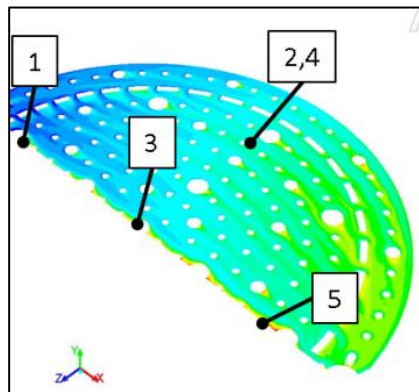


Figure 32: CFD results for pressure cooling capacity and thermal distribution

The thermal profile was evaluated first to ensure the prototypes were fabricated correctly and they would function properly for all experiments. Flow distribution was

measured during the cooling capacity tests by attaching thermocouples to the surface of each cooling plate. A resistive heater was placed on the opposite side of the cooling plate to apply the heat load. The temperatures of each of the thermocouples were measured once the cooling plate reached a steady state condition with 52 W applied with a flow rate of 149 mL/min. The relative temperature was used to show the flow distribution. Thermocouples 1, 3, and 5 showed the thermal profile cooling fluid across the plate, while thermocouples 2, 3, and 4 showed how well the fluid was distributed perpendicular to the flow path (e.g. if the fluid was evenly distributed across the whole flow channel). The first results were obtained to view the grouping of the thermal readings. It was expected that with an inlet temperature of 290.8 K, the temperature profile should be linear and the outlet would be around 295.8 K.

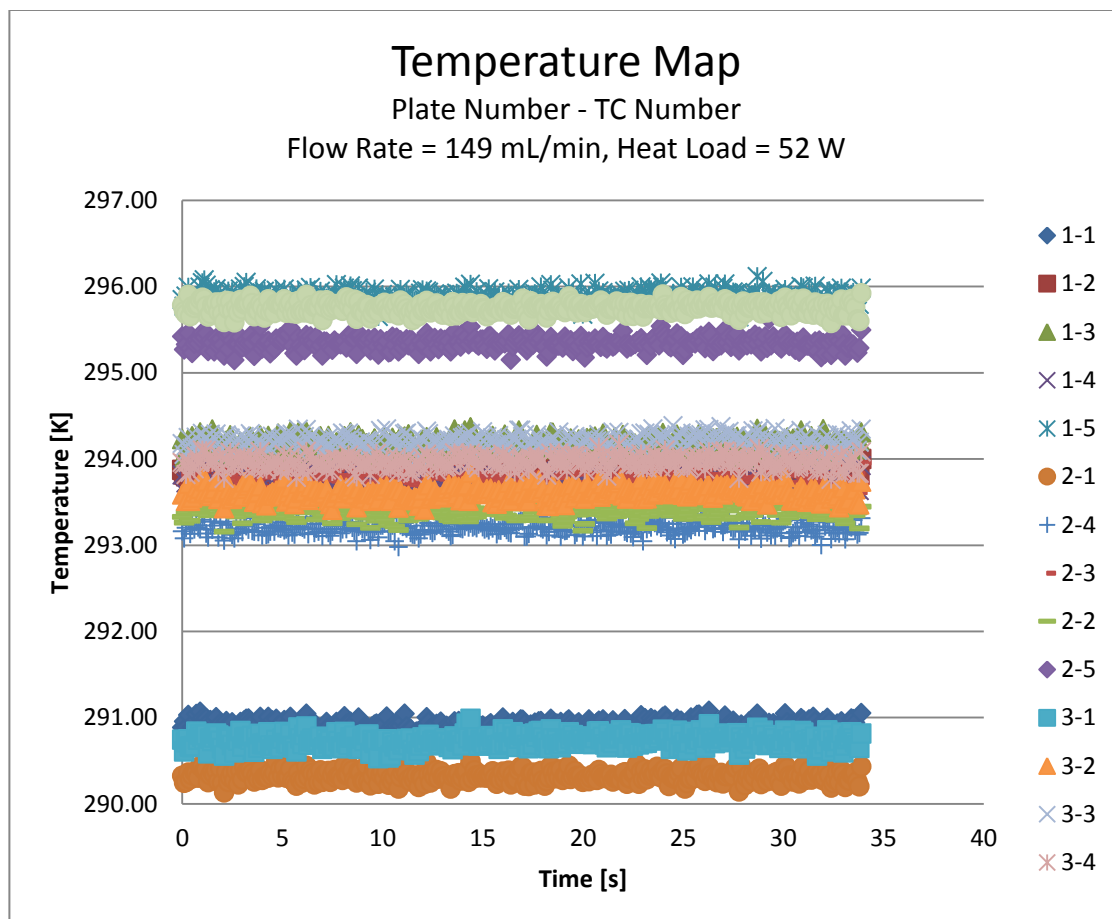


Figure 33: Thermal results showing the thermocouple groupings

The thermocouple temperature map shown above was as expected. Inlet thermocouples (X-1) had the lowest temperature while the outlet thermocouples (X-5) had the highest temperature. With an inlet temperature of 291 K average across the plates, the average outlet temperature was 296 K. The middle thermocouples (X-2, X-3, X-4) were uniformly grouped and were slightly higher than the expected value of 293.5 K.

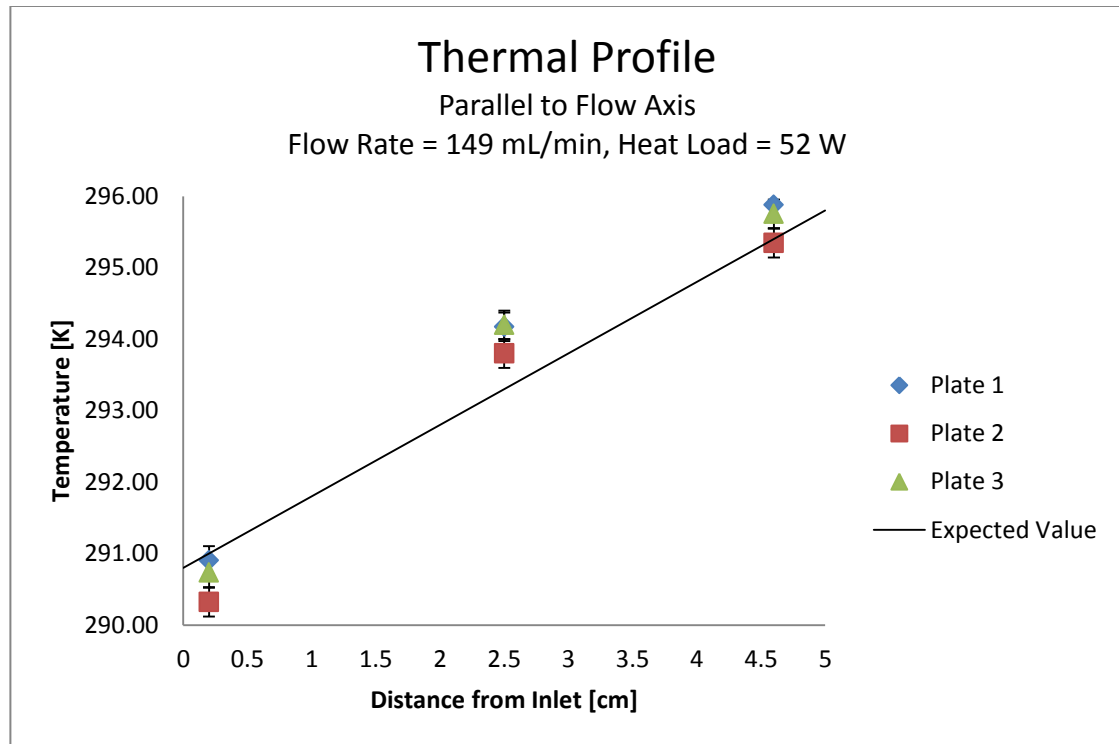


Figure 34: Thermal profile showing flow distribution of the cooling plates parallel to the flow path

As shown in Figure 34, the thermal profile down the flow axis (from inlet to outlet) shows good agreement with the expected results. From inlet to outlet, the temperature gradient was found to be around 5 K which is consistent with calculations in section 4.2. Error bars show the standard error of the thermocouples. The central thermocouples (position 3), showed a higher value than expected. This is likely due to their placement directly over the heat sheets compared with thermocouples 1, 2, 4 and 5 which are near the periphery of the heat sheets since it is square. Despite this, results show an increasing temperature gradient close to what was expected.

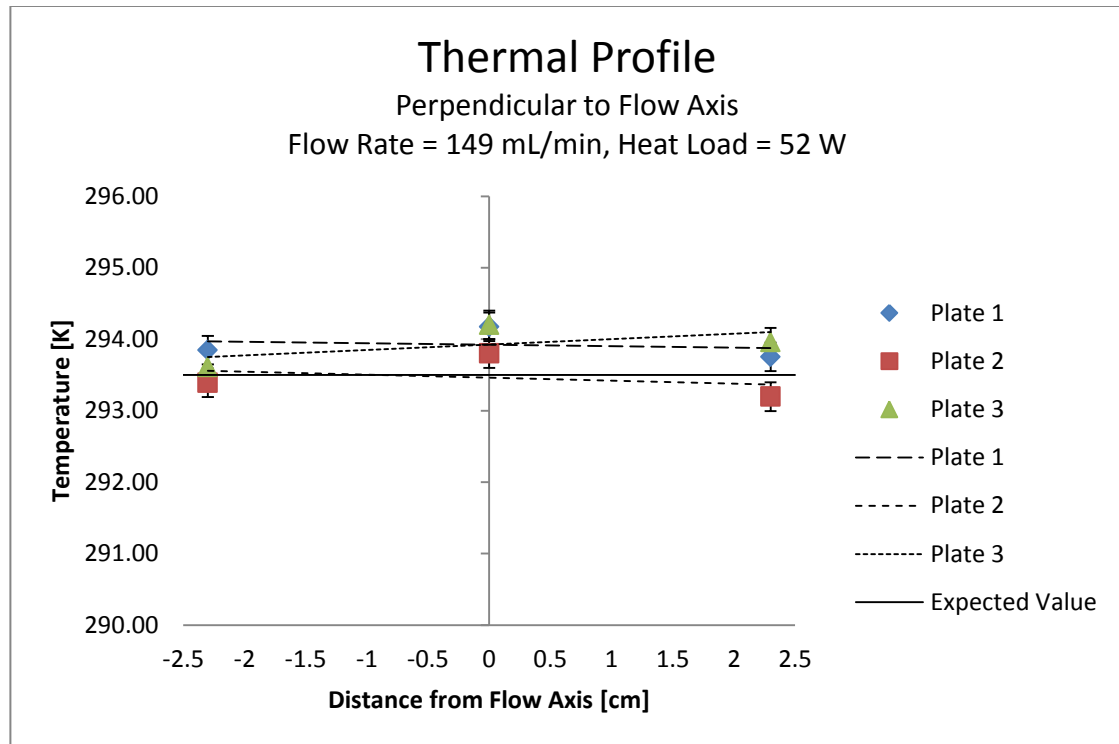


Figure 35: Thermal profile showing flow distribution of the cooling plates perpendicular to the flow path

Figure 35 shows the temperature profile perpendicular to the flow axis suggesting a fairly uniform temperature distribution across each of the three plates. In addition, the data clearly shows that flow distribution between plates was not an issue. Plate 1 had a temperature distribution very similar to that of plate 3 with some values on Plate 1 actually higher than those of plate 3. Experimental temperatures are compared with expected results based on CFD which showed a temperature of 293.6 K across the centerplane of the plate. Similar to Figure 34, Figure 35 shows that thermocouple 3 for each plate has a slightly higher value. For each location, temperatures are within about 0.5 K of each other, showing fairly good agreement. The slight difference could be due to thermocouple placement with respect to the heater, placement quality on the cooling plate surface, or out of parallelism of the cooling plates which could cause flow maldistribution.

The flow distribution results show that the fluid distribution is good in both directions: with the flow path and perpendicular to the flow path. This suggests each cooling plate has fluid flowing evenly throughout the channels and that the fluid was evenly distributed to each channel as well. The results also show that the header sizing lead to even distribution of fluid to each of the cooling plates because the temperature between the plates are similar and are close to the error limits of the thermocouples (± 0.2 °K). The error bars show the standard error of the thermocouples.

Experimental cooling capacity results were obtained by measuring the temperature difference from the inlet to the outlet using the thermocouples and calculating the cooling capacity at a given flow rate. The temperature difference for various flow rates were found as follows (Figure 36).

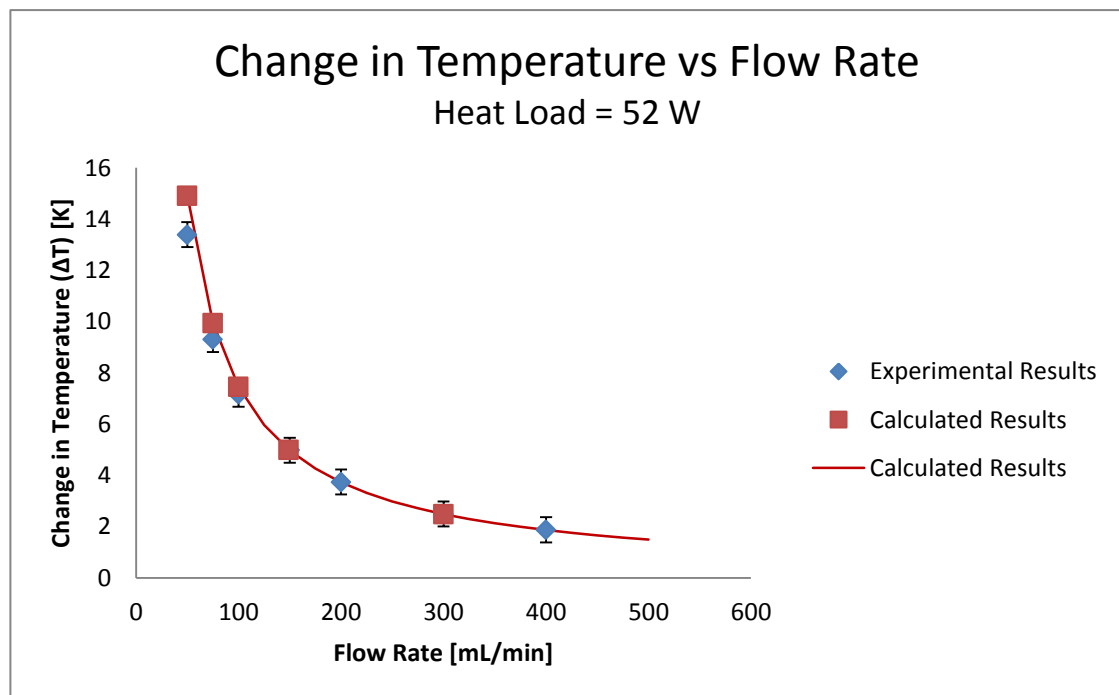


Figure 36: Temperature difference due to an applied heat load of 52 W at various flow rates

Figure 36 shows that the temperature changes with flow rate. The required flow rate was calculated as 149 mL/min to remove the 52 W across the three plates. Beyond this point, the experimental temperature has good agreement with the calculated temperature required to remove 52 W. However, before this point, it was observed that the temperature deviates from the expected values. This means that heat is being lost either through axial conduction through the MATI or through the insulation. With the obtained temperature values, the cooling capacity was calculated (Figure 37).

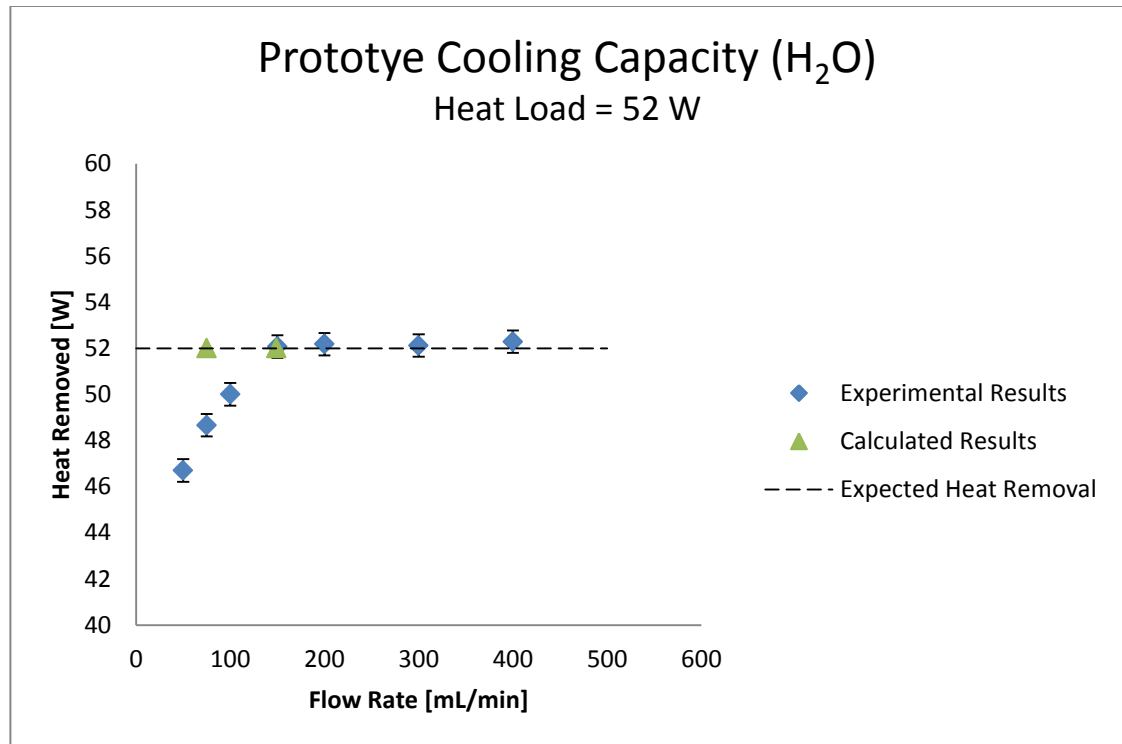


Figure 37: Cooling capacity results

Results show that the heat was effectively removed at flow rates of 149 mL/min and beyond which is in agreement with calculations. Below a flow rate of 149 mL/min, the microchannels are not picking up enough heat, which is being lost by either axial conduction

or heat loss through the insulation. The error bars were found from the standard deviation between four test runs.

The MATI pressure drop was found by measuring the differential pressure across the MATI at various flow rates. The test setup included several expansions and contractions before the inlet and after the outlet to enable connections to the pressure transducers. To quantify the pressure drop due to these expansions and contractions, a tube of known diameter and length was inserted between the test setup headers and pressure drop measurements were obtained. The pressure drop due to the tube was removed from the setup pressure drop measurements to quantify the baseline pressure drop. Therefore, to determine the pressure drop through the MATI prototype, these baseline pressure drops were removed as a function of flow rate. The resulting pressure drop through the MATI prototype is shown in [Figure 38](#) as a function of flow rate.

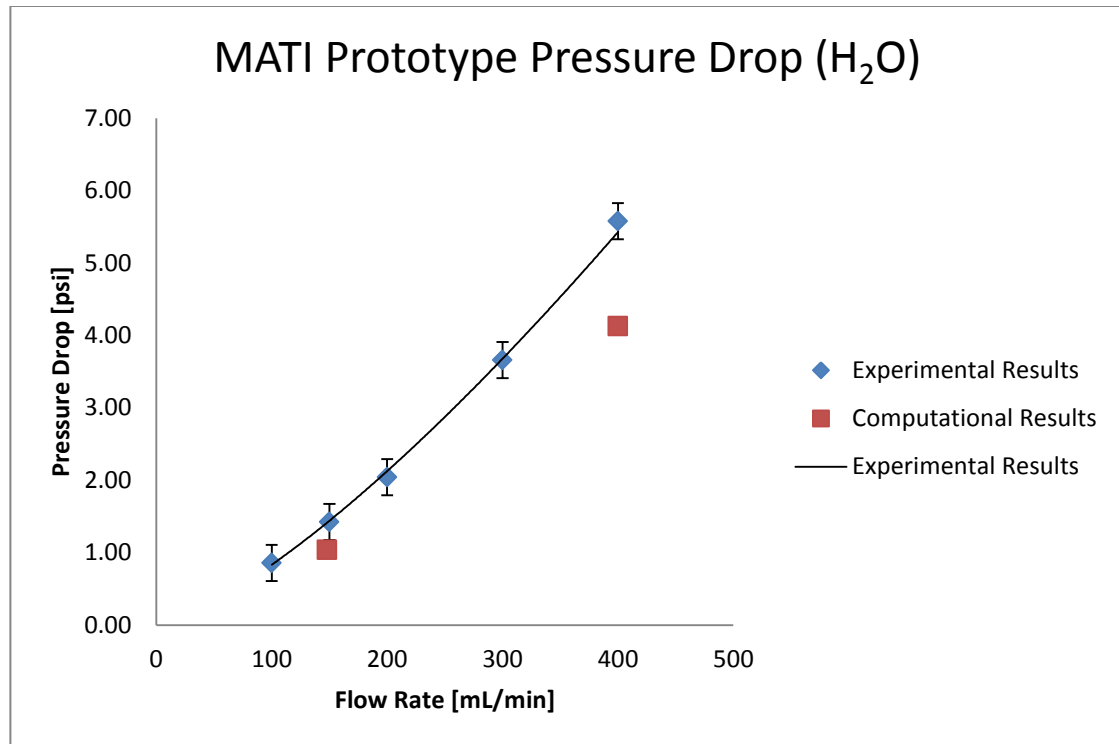


Figure 38: Pressure drop results of the MATI prototype

In Figure 38, the expected pressure drop of the cooling plate was plotted for comparison with experimental results. The expected pressure drop of the cooling plate was determined by adding the pressure drop of the plate estimated by CFD with the calculated pressure drop of the header. Expected values were 1.03 psi and 4.13 psi for flow rates of 150 and 400 mL/min, respectively. Experimental results showed that the MATI prototype had a pressure drop of 1.42 psi and 5.58 psi for flow rates of 150 and 400 mL/min yielding experimental errors of 27% and 26%, respectively. A significant portion of these differences can be explained by the parallelism error noted in the fabrication section. During the bonding process, creeping of the lamina over unsupported regions caused a deflection of the upper lamina into the channel resulting in a slight (but uniform) decrease in channel height

(13 μm) of 5% on average. Using pressure drop as a function of flow rate, the hydraulic diameter is related to pressure drop by a relationship of $1/D^4$. Consequently, a 5% reduction in the hydraulic diameter would yield approximately a 22.8% increase in pressure drop. The remainder of the difference can be explained by the prototypes having filleted edges due to PCM which further reduce the hydraulic diameter. The error bars represent the error of the pressure transducers (± 0.25 psi).

5.2 Thermal Stress Evaluation

Per the experimental protocol, the two successful prototypes were submerged 10 times in liquid nitrogen from room temperature with no observable failures afterwards during hermetic testing. Next, the two prototypes were setup on the cryogenic test loop and liquid nitrogen was run through the channels for 5 minutes without hermetic failure. Afterward, the MATI prototypes were left on the experimental setup overnight to heat back up to ambient temperature so as to not cause any failures in the cryogenic test setup. Again, the prototypes were subjected to hermeticity testing without failure. Throughout testing, no observable changes in the geometry of the prototypes were observed. These results suggest that thermal shock is not a concern in the MATI prototypes since the maximum tank temperatures are expected to be only 160 K, suggesting maximum temperature gradients of 90 K compared to the temperature gradients of 220 K experienced in these tests.

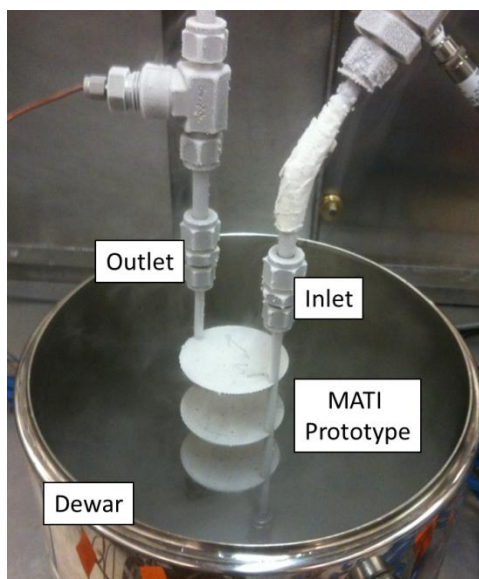


Figure 39: LN2 flow through test

6. CONCLUSIONS

In this paper, a Modular Adsorption Tank Insert (MATI) was described for managing the heat of adsorption within adsorptive hydrogen storage schemes. The MATI was designed to remove the heat of adsorption from adsorptive materials during the filling of onboard storage tanks for light duty vehicles. Through the use of microchannel cooling plates, the system was developed to minimize displacement volume within the tank. System models were shown that the system can store 5.6 kg of H_2 using a MATI system occupying less than 6.3% of the internal tank volume. The MATI system has 10% less displacement volume than other heat exchangers developed for metal hydride storage systems.

CFD and FEA models were used to evaluate the design and sub-scale prototypes were fabricated to validate the models. A 316 stainless steel prototype was developed to validate flow and thermal distribution within the system and to investigate the thermal

effects of cryogenic operation. The prototype was produced using photochemical machining, diffusion bonding, laser cutting and brazing techniques similar to those used to manufacture automotive radiators. Cost models show that at a production volume of 500,000 MATIs per year, the cost of goods sold is expected to be around \$780 per MATI unit. Additional efforts are needed to reduce the cost of the system using cheaper materials.

Models and experiments showed that the design provides good fluid distribution between and across the plates with acceptable pressure drop through the system. Further, the results suggest the MATI has the cooling capacity to effectively remove the heat of adsorption with a minimal displacement volume and can withstand the thermal effects of cryogenic storage.

BIBLIOGRAPHY

- [1] S. Davis, S. Diegel and R. Boundy, "Transportation Energy Data Book, 30th Ed.," U.S. Department of Energy, Energy Efficiency & Renewable Energy, Oak Ridge National Laboratory, Oak Ridge, TN, 2011.
- [2] "Just the Basics - Fuel Cells," U.S. Department of Energy, Argonne National Laboratory, 2010. [Online]. Available: <http://www.transportation.anl.gov/pdfs/FC/521.PDF>. [Accessed 15 February 2012].
- [3] "U.S. Imports by Country of Origin - Crude Oil," U.S. Energy Information Administration, 2012. [Online]. Available: http://205.254.135.7/dnav/pet/pet_move_impcus_a2_nus_epc0_im0_mbb1_m.htm. [Accessed 14 February 2012].
- [4] J. Holladay, J. Hu, D. King and Y. Wang, "An overview of hydrogen production technologies," *Catalysis Today*, vol. 139, pp. 244-260, 2009.
- [5] "Hydrogen Posture Plan," U.S. Department of Energy, Hydrogen and Fuel Cells Program, 2006. [Online]. Available: http://www.hydrogen.energy.gov/pdfs/hydrogen_posture_plan_dec06.pdf. [Accessed September 2011].
- [6] "Hydrogen and Fuel Cells Program Plan," U.S. Department of Energy, Hydrogen and Fuel Cells Program, 2011. [Online]. Available: http://www1.eere.energy.gov/hydrogenandfuelcells/pdfs/program_plan2011.pdf. [Accessed December 2011].
- [7] "A National Vision of America's Transition to a Hydrogen Economy - To 2030 and Beyond," U.S. Department of Energy, Hydrogen and Fuel Cells Program Plan, 2002. [Online]. Available: http://hydrogen.energy.gov/pdfs/vision_doc.pdf. [Accessed September 2011].
- [8] "National Hydrogen Energy Roadmap," U.S. Department of Energy, Hydrogen and Fuel Cells Program, 2002. [Online]. Available: http://www.hydrogen.energy.gov/pdfs/national_h2_roadmap.pdf. [Accessed September 2011].

- [9] "Hydrogen Potential from Solar and Wind Resources - Record #5011," U.S. Department of Energy, Hydrogen and Fuel Cells Program, 2005. [Online]. Available: http://www.hydrogen.energy.gov/pdfs/5011_h2_potential_solar_wind.pdf. [Accessed September 2011].
- [10] R. Ahluwalia and X. Wang, "Fuel cell systems for transportation: Status and trends," *Journal of Power Sources*, vol. 177, pp. 167-176, 2008.
- [11] "Well-to-Wheel Energy Use and Greenhouse Gas Emissions of Advanced Fuel/Vehicle Systems - North American Analysis," U.S. Department of Energy, Hydrogen and Fuel Cells Program, 2001. [Online]. Available: http://www.fischer-tropsch.org/DOE/DOE_reports/10556/ANL-ES-RP-10556,%2008-23-01.pdf. [Accessed September 2011].
- [12] "Multi-Year Research, Development and Demonstration Plan; Technical Plan - Manufacturing," U.S. Department of Energy, Hydrogen and Fuel Cells Program, 2011. [Online]. Available: <http://www1.eere.energy.gov/hydrogenandfuelcells/mypp/index.html>. [Accessed December 2011].
- [13] G. Thomas and J. Keller, "Hydrogen Storage - Overview," U.S. Department of Energy, Office of Energy Efficiency and Renewable Energy, 2003. [Online]. Available: http://www1.eere.energy.gov/hydrogenandfuelcells/pdfs/bulk_hydrogen_stor_pres_sandia.pdf. [Accessed 10 March 2012].
- [14] "Targets for Onboard Hydrogen Storage Systems for Light-Duty Vehicles," U.S. Department of Energy, Office of Energy Efficiency and Renewable Energy, [Online]. Available: http://www1.eere.energy.gov/hydrogenandfuelcells/storage/pdfs/targets_onboard_hydro_storage_explanation.pdf. [Accessed September 2011].
- [15] A. Zuttel, "Materials for hydrogen storage," *Materials Today*, pp. 24-33, September 2003.
- [16] M. Felderhoff, C. Weidenthaler, R. von Helmolt and U. Eberle, "Hydrogen storage: the remaining scientific and technological challenges," *Physical Chemistry Chemical Physics*, vol. 9, pp. 2643-2653, 2007.
- [17] B. Hassel, J. Pasini, M. Gorbounov, J. Holowczak, I. Fedchenia, J. Khalil, F. Sun, X. Tang, R. Brown, L. Pryor and B. Laube, "Advancement of Systems Designs and Key Engineering

Technologies for Materials-Based Hydrogen Storage," U.S. Department of Energy Hydrogen and Fuel Cells Program, 2011.

- [18] T. Hua, R. Ahluwalia, J. Peng, M. Kromer, S. Lasher, K. McKenney, K. Law and J. Sinha, "Technical assessment of compressed hydrogen storage tank systems for automotive applications," *International Journal of Hydrogen Energy*, vol. 36, pp. 3037-3049, 2011.
- [19] U. Eberle, M. Felderhoff and F. Schuth, "Chemical and Physical Solutions for Hydrogen Storage," *Angewandte Chemie*, vol. 48, pp. 6608-6630, 2009.
- [20] P. Jena, "Materials for Hydrogen Storage: Past, Present, and Future," *The Journal of Physical Chemistry Letters*, vol. 2, pp. 206-211, 2011.
- [21] R. Ahluwalia, T. Hua, J. Peng, S. Lasher, K. McKenney, J. Sinha and M. Gardiner, "Technical assessment of cryo-compressed hydrogen storage tank systems for automotive applications," *International Journal of Hydrogen Energy*, vol. 35, pp. 4171-4184, 2010.
- [22] R. Ahluwalia, T. Hua, J. Peng, S. Lasher, K. McKenney and J. Sinha, "Technical Assessment of Cryo-Compressed Hydrogen Storage Tank Systems for Automotive Applications," Nuclear Engineering Department, Argonne National Laboratory, Argonne, IL, 2009.
- [23] R. Ahluwalia and J. Peng, "Dynamics of cryogenic hydrogen storage in insulated pressure vessels for automotive applications," *International Journal of Hydrogen energy*, vol. 33, pp. 4622-4633, 2008.
- [24] Weidenthaler, C. and Felderhoff, M., "Solid-state hydrogen storage for mobile applications: Quo Vadis?," *Energy & Environmental Science*, vol. 4, pp. 2495-2502, 2011.
- [25] B. Hands, *Cryogenic Engineering*, Orlando, FL: Academic Press, 1986.
- [26] P. Benard and R. Chahine, "Modeling of adsorption storage of hydrogen on activated carbons," *International Journal of Hydrogen Energy*, vol. 26, pp. 849-855, 2001.
- [27] J. Rosenfeld and K. Law, "Cost Analysis of Hydrogen Storage Materials and On-Board Materials," U.S. Department of Energy, Annual Merit Review, 2011. [Online]. Available: http://www.hydrogen.energy.gov/pdfs/review11/st002_law_2011_o.pdf. [Accessed 14 May 2012].

- [28] R. Biniwale, S. Rayalu, S. Devotta and M. Ichikawa, "Chemical hydrides: A solution to high capacity hydrogen storage and supply," *International Journal of Hydrogen Energy*, vol. 33, pp. 360-365, 2007.
- [29] B. Sakintuna, F. Lamari-Darkrim and M. Hirscher, "Metal hydride materials for solid hydrogen storage: A review," *International Journal of Hydrogen Energy*, vol. 32, pp. 1121-1140, 2007.
- [30] I. Jain, L. Chhagan and A. Jain, "Hydrogen storage in Mg: A most promising material," *International Journal of Hydrogen Energy*, vol. 35, pp. 5133-5144, 2009.
- [31] J. Zhang and T. Fisher, "A Review of Heat Transfer Issues in Hydrogen Storage Technologies," *Journal of Heat Transfer*, vol. 127, pp. 1391-1399, 2005.
- [32] R. Bowman and N. Stetson, "Hydrogen Storage Materials: 2007-2009 - Record #9014," U.S. Department of Energy, Hydrogen and Fuel Cells Program, 2009. [Online]. Available: http://www.hydrogen.energy.gov/pdfs/9014_hydrogen_storage_materials.pdf. [Accessed September 2011].
- [33] K. Lim, H. Kazemian, Z. Yaakob and W. Daud, "Solid-state Materials and Methods for Hydrogen Storage: A Critical Review," *Chemical Engineering & Technology*, vol. 33, pp. 213-226, 2010.
- [34] M. Richard, D. Cossment, P. Chandonia and R. Chahine, "Preliminary Evaluation of the Performance of an Adsorption-Based Hydrogen Storage System," *AIChE Journal*, vol. 55, no. 11, pp. 2985-2996, 2009.
- [35] A. Dillon and M. Heben, "Hydrogen storage using carbon adsorbents: past, present and future," *Applied Physics A*, vol. 72, pp. 133-142, 2001.
- [36] R. Ahluwalia and J. Peng, "Automotive hydrogen storage system using cryo-adsorption on activated carbons," *International Journal of Hydrogen Energy*, vol. 34, pp. 5476-5487, 2009.
- [37] M. Rzepka, P. Lamp and M. de la Casa-Lillo, "Physisorption of Hydrogen on Microporous Carbon and Carbon Nanotubes," *Journal of Physical Chemistry B*, vol. 102, pp. 10894-10898, 1998.
- [38] M. Niemann, S. Srinivasan, A. Phani, A. Kumar, D. Goswami and E. Stefanakos, "Nanomaterials for Hydrogen Storage Applications: A Review," *Journal of*

Nanomaterials, no. 950967, pp. 1-9, 2008.

- [39] P. Benard, R. Chahine, P. Chandonia, D. Cossement, G. Dorval-Douville, L. Lafi, P. Lachance, R. Paggiaro and E. Poirier, "Comparison of hydrogen adsorption on nanoporous materials," *Journal of Alloys and Compounds*, Vols. 446-447, pp. 380-384, 2007.
- [40] Y. Hu and L. Zhang, "Hydrogen Storage in Metal-Organic Frameworks," *Advanced Energy Materials*, vol. 22, pp. E117-E130, 2010.
- [41] J. Sculley, D. Yuan and H. Zhou, "The current status of hydrogen storage in metal-organic frameworks - updated," *Energy & Environmental Science*, vol. 4, pp. 2721-2735, 2011.
- [42] S. Han, H. Furukawa, O. Yaghi and W. Goddard III, "Covalent Organic Frameworks as Exceptional Hydrogen Storage Materials," *Journal of the American Chemical Society*, vol. 130, no. 35, pp. 11580-11581, 2008.
- [43] E. Klontzas, E. Tylianakis and G. Froudakis, "Designing 3D COFs with Enhanced Hydrogen Storage Capacity," *Nano Letters*, vol. 10, pp. 452-454, 2010.
- [44] S. Bhatia and A. Myers, "Optimum Conditions for Adsorptive Storage," *Langmuir*, vol. 22, no. 4, pp. 1688-1700, 2006.
- [45] B. Kuchta, L. Firlej, P. Pfeifer and C. Wexler, "Numerical estimation of hydrogen storage limits in carbon-based nanospaces," *Carbon*, vol. 48, pp. 223-231, 2010.
- [46] V. Fierro, A. Szczurek, C. Zlotea, J. Mareche, M. Izquierdo, A. Albinia, M. Latroche, G. Furdin and A. Celzard, "Experimental evidence of an upper limit for hydrogen storage at 77 K on activated carbons," *Carbon*, vol. 48, pp. 1902-1911, 2010.
- [47] B. Weinberger and F. Darkim-Lamari, "High pressure cryo-storage of hydrogen by adsorption at 77 K and up to 50 MPa," *International Journal of Hydrogen Energy*, vol. 34, pp. 3058-3064, 2009.
- [48] K. Thomas, "Hydrogen adsorption and storage on porous media," *Catalysis Today*, vol. 120, pp. 389-398, 2007.
- [49] M. Lamari, A. Aoufi and P. Malbrunot, "Thermal Effects in Dynamic Storage of Hydrogen by Adsorption," *AIChE Journal*, vol. 46, no. 3, pp. 632-646, 2000.

- [50] G. Hermosilla-Lara, G. Momen, P. Marty, B. Le Neindre and K. Hassouni, "Hydrogen storage by adsorption on activated carbon: Investigation of the thermal effects during the charging process," *International Journal of Hydrogen Energy*, vol. 32, pp. 1542-1553, 2007.
- [51] M. Visaria, I. Mudawar and T. Pourpoint, "Enhanced heat exchanger design for hydrogen storage using high-pressure metal hydride: Part 1. Design methodology and computational results," *International Journal of Heat and Mass Transfer*, vol. 54, pp. 413-423, 2011.
- [52] M. Raju and S. Kumar, "Optimization of heat exchanger designs in metal hydride based hydrogen storage systems," *International Journal of Hydrogen Energy*, vol. 37, pp. 2767-2778, 2012.
- [53] M. Visaria and I. Mudawar, "Coiled-tube heat exchanger for High-Pressure Metal Hydride hydrogen storage systems – Part 1. Experimental study," *International Journal of Heat and Mass Transfer*, vol. 55, pp. 1782-1795, 2012.
- [54] B. Paul, "Micro energy and chemical systems and multi-scale fabrication," in *Micromanufacturing and Nanotechnology, 1st Ed.*, vol. 1, Berlin, Germany, Springer-Verlag, 2006, pp. 323-352.
- [55] S. Leith, D. King and B. Paul, "Toward Low-Cost Fabrication of Microchannel Process Technologies - Cost Modeling for Manufacturing Development," in *AIChE Annual Meeting*, Salt Lake City, UT, 2010.
- [56] B. Lajevardi, S. Leith, D. King and B. Paul, "Arrayed Microchannel Manufacturing Costs for an Auxiliary Power Unit Heat Exchanger," in *Proceedings of the Industrial Engineering Research Conference*, 2011.
- [57] C. Loeb, A. Truszkowska and G. Jovanovic, "Removal of heat from a hydrogen storage media by a novel microscale-based heat exchanger," in *World Hydrogen Energy Conference*, Toronto, Canada, 2012.
- [58] A. Truszkowska and G. Jovanovic, "Temperature Distribution in Activated Carbon Bed During Adsorption of Nitrogen," in *American Institute of Chemical Engineers*, Minneapolis, MN, 2011.
- [59] "Technical Reference for Hydrogen Compatibility of Materials," Sandia National Laboratory, 2008. [Online]. Available: <http://www.sandia.gov/matlsTechRef/>. [Accessed

September 2011].

- [60] M. McClintock, *Cryogenics*, New York, NY: Reinhold Publishing, 1964.
- [61] E. Herms, J. Olive and M. Puiggali, "Hydrogen embrittlement of 316L type stainless steel," *Materials Science and Engineering*, vol. 272, pp. 279-283, 1999.
- [62] P. Sofronis and I. Robertson, "Viable Mechanisms of Hydrogen Embrittlement - A Review," in *Second International Symposium on Hydrogen in Matter*, Uppsala, Sweden, 2005.
- [63] T. Ogata, "HYDROGEN EMBRITTLEMENT EVALUATION IN TENSILE PROPERTIES OF STAINLESS STEELS AT CRYOGENIC TEMPERATURES," *Transactions of the International Cryogenic Materials Conference*, vol. 54, pp. 124-131, 2008.
- [64] G. Nellis, *Heat Transfer*, Cambridge, UK: Cambridge University Press, 2008.
- [65] R. Powell, C. Ho and P. Liley, "Thermal Conductivity of Selected Materials," 25 November 1966. [Online]. Available: <http://www.nist.gov/data/nsrds/NSRDS-NBS-8.pdf>. [Accessed 05 06 2012].
- [66] H. Johnston and E. Long, "Heat Capacity Curves of the Simpler Gases. VI.," *Journal of Physical Chemistry*, vol. 2, pp. 389-395, 1934.
- [67] K. Drost, "Microscale Enhancement of Heat and Mass Transfer for Hydrogen Energy Storage," U.S. Department of Energy, Annual Merit Review, 15 May 2012. [Online]. Available: http://www.hydrogen.energy.gov/pdfs/review12/st046_drost_2012_o.pdf. [Accessed 25 May 2012].
- [68] R. Roark and W. Young, *Roark's Formulas for Stress and Strain*, 6th Ed., New York, NY: McGraw-Hill, 1989.
- [69] AWS C3.3:2002 - Recommended Practices for the Design, Manufacture, and Examination of Critical Braze Components, American Welding Society, 2002.
- [70] AWS Brazing Handbook, 4th Ed., Miami, FL: American Welding Society, 1991.
- [71] V. Hessel, A. Renken, J. Schouten and J. Yoshida, *Micro Process Engineering: A Comprehensive Handbook*, Volume 1, Wiley-VCH Verlag GmbH & Co., 2009.

- [72] D. Read and R. Reed, "Fracture and strength properties of selected austenitic stainless steels as cryogenic temperatures," *Cryogenics*, vol. 21, no. 7, pp. 415-417, 1981.
- [73] T. Siewert, C. McCowan and D. Vigliotti, "Cryogenic material properties of stainless steel tube-to-flange welds," *Cryogenics*, vol. 30, no. 4, pp. 356-364, 1990.
- [74] P. Paulraj and B. Paul, "MICROCHANNEL STRUCTURES HAVING BONDED LAYERS INCLUDING HEIGHT CONTROL FEATURES". United States of America Patent 20100254858, 7 October 2010.
- [75] O. Yaghi, "Hydrogen Storage in Metal-Organic Frameworks," U.S. Department of Energy Hydrogen and Fuel Cells Program, 2011.
- [76] K. Drost, G. Jovanovic, V. Narayanan, B. Paul, A. Garrison, K. Schilke, C. Loeb, L. Steigleder, D. Haley, M. Ghavzini and A. Truszkowska, "Microscale Enhancement of Heat and Mass Transfer for Hydrogen Energy Storage," U.S. Department of Energy Hydrogen and Fuel Cells Program, 2011.
- [77] D. Jacobson, Principles of Brazing, Materials Park, NY: ASM International, 2005.
- [78] T. Ogata, T. Yuri and Y. Ono, "TENSILE PROPERTIES, FERRITE CONTENTS, AND SPECIMEN HEATING OF STAINLESS STEELS IN CRYOGENIC ENVIRONMENTS," *Transactions of the International Cryogenic Materials Conference*, vol. 52, pp. 122-129, 2006.
- [79] S. Mellouli, H. Dhaou, F. Askri, A. Jemni and S. Nasrallah, "Hydrogen storage in metal hydride tanks equipped with metal foam heat exchanger," *International Journal of Hydrogen Energy*, vol. 34, pp. 9393-9401, 2009.

APPENDICES

APPENDIX A: DOE TECHNICAL HYDROGEN STORAGE TARGETS

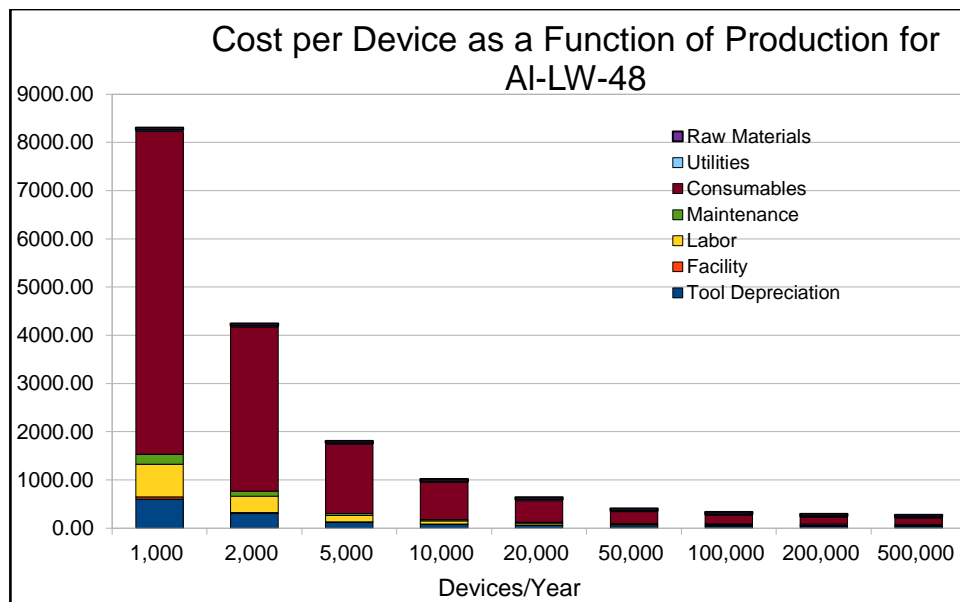
DOE Targets for Onboard Hydrogen Storage Systems for Light-Duty Vehicles

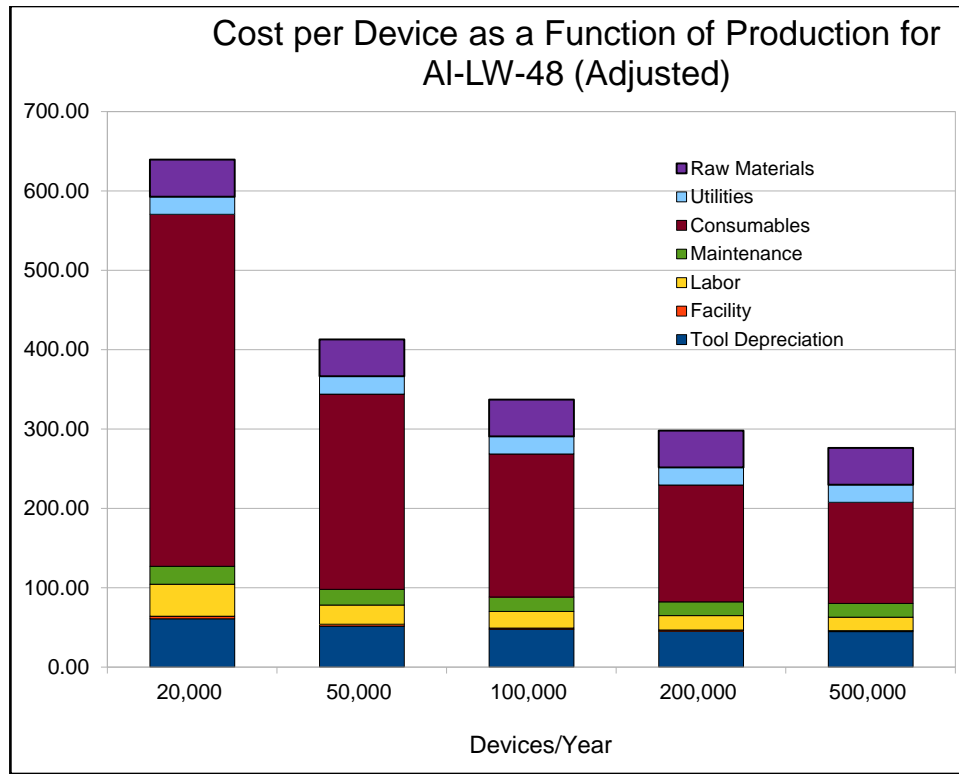
Table 2 Technical Targets: Onboard Hydrogen Storage Systems				
Storage Parameter	Units	2010	2017	Ultimate
System Gravimetric Capacity: Usable, specific-energy from H ₂ (net useful energy/max system mass) ^a	kWh/kg (kg H ₂ /kg system)	1.5 (0.045)	1.8 (0.055)	2.5 (0.075)
System Volumetric Capacity: Usable energy density from H ₂ (net useful energy/max system volume)	kWh/L (kg H ₂ /L system)	0.9 (0.028)	1.3 (0.040)	2.3 (0.070)
Storage System Cost ^b :	\$/kWh net (\$/kg H ₂)	TBD (TBD)	TBD (TBD)	TBD (TBD)
• Fuel cost ^c	\$/gge at pump	3-7	2-4	2-4
Durability/Operability:				
• Operating ambient temperature ^d	°C	-30/50 (sun)	-40/60 (sun)	-40/60 (sun)
• Min/max delivery temperature	°C	-40/85	-40/85	-40/85
• Operational cycle life (1/4 tank to full) ^e	Cycles	1000	1500	1500
• Min delivery pressure from storage system; FC= fuel cell, ICE= internal combustion engine	bar (abs)	5 FC/35 ICE	5 FC/35 ICE	3 FC/35 ICE
• Max delivery pressure from storage system ^f	bar (abs)	12 FC/100 ICE	12 FC/100 ICE	12 FC/100 ICE
• Onboard Efficiency	%	90	90	90
• "Well" to Powerplant Efficiency	%	60	60	60
Charging / Discharging Rates:				
• System fill time (5 kg)	min (kg H ₂ /min)	4.2 (1.2)	3.3 (1.5)	2.5 (2.0)
• Minimum full flow rate	(g/s)/kW	0.02	0.02	0.02
• Start time to full flow (20°C) ^g	s	5	5	5
• Start time to full flow (-20°C) ^g	s	15	15	15
• Transient response 10%-90% and 90% - 0% ^h	s	0.75	0.75	0.75
Fuel Purity (H ₂ from storage) ⁱ :	% H ₂	SAE J2719 and ISO/PDTS 14687-2 (99.97% dry basis)		
Environmental Health & Safety:				
• Permeation & leakage ^j	Scch/h	Meets or exceeds applicable standards		
• Toxicity	-			
• Safety	-			
• Loss of useable H ₂ ^k	(g/h)/kg H ₂ stored	0.1	0.05	0.05

Useful constants: 0.2778 kWh/MJ; 33.3 kWh/kg H₂; 1 kg H₂ ≈ 1 gal gasoline equivalent.

Source: DOE 2011,

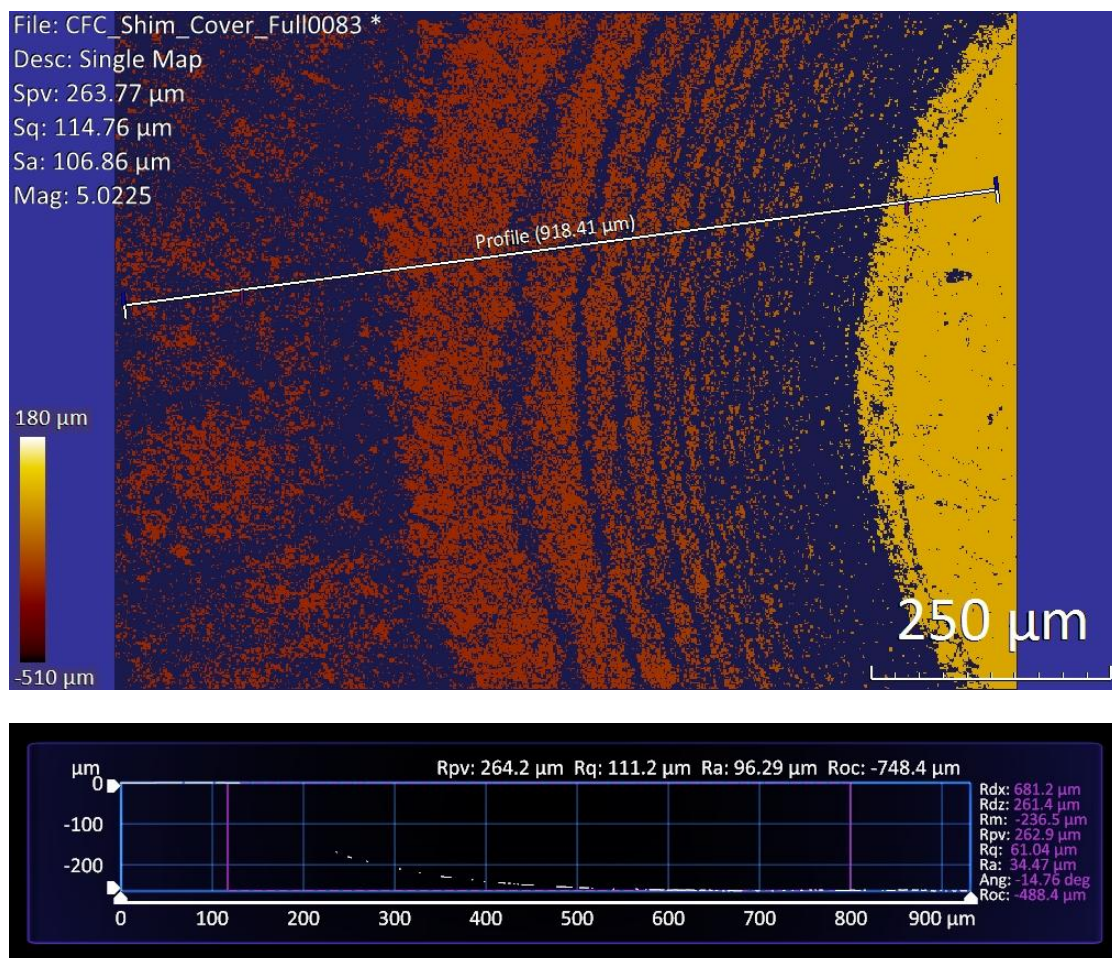
http://www1.eere.energy.gov/hydrogenandfuelcells/storage/pdfs/targets_onboard_hydro_storage_explanation.pdf





These results show a cost reduction strategy by selecting 3000 series aluminum as the raw material and using laser welding as the bonding method. With the shown changes, costs for the MATI were able to be reduced to \$290 per system. Further cost reductions could be noticed by changing the forming process to stamping from PCM. Raw materials costs would be reduced by increasing materials utilization with the near net process forming technique and consumables would be dramatically reduced.

APPENDIX C: SHIM CHARACTERIZATION



Screen shot of etch depth measurements from the ZeScope showing an etch depth of 261.4 μm .

A total of three shims were evaluated with 15 measurements taken from each shim for a total of 45 measurements. An average of 261.3 μm was found with a standard deviation of 9.1 μm .